IMMUNOLOGY

Human NLRP3 inflammasome activation leads to formation of condensate at the microtubule organizing center

Jue Wang[1,2], Man Wu[3,4], Le Xiao[3,4], Gang Du[3,4]†, Muyuan Chen[2], Venkat G. Magupalli[3,4]‡, Peter D. Dahlberg[2]*, Hao Wu[3,4]*, Grant J. Jensen[5]*

The NLRP3 inflammasome is a multiprotein molecular machine that drives inflammatory responses in innate immunity. Although its dysregulation is implicated in numerous human diseases, its structural organization in cells remains poorly understood. Here, we used precise fluorescence-guided cryo–focused ion beam (cryo-FIB) milling and cryo–electron tomography (cryo-ET) to visualize NLRP3 inflammasomes in situ within human macrophages at various stages of activation. After priming and activation, we observed expansion and dispersion of Golgi cisternae, along with the emergence of 50-nanometer NLRP3-associated vesicles, which likely transport NLRP3 to the MTOC. Dense NLRP3-containing condensates then formed in and around the MTOC. In later stages, the condensates solidified, coincident with widespread mitochondrial damage, autophagy, and pyroptotic cell death.

INTRODUCTION

Canonical inflammasomes are cytoplasmic, supramolecular complexes responsible for detecting and sensing infections and cellular distress (*1*–*3*). Upon activation, these multiprotein complexes activate procaspases, release inflammatory cytokines, and eventually cause pyroptotic cell death (*1*–*3*). One of the most extensively studied members in this family, the NLRP3 inflammasome, is composed of an NLRP3 sensor protein (also known as cryopyrin), an apoptosis-associated speck-like protein containing a C-terminal caspase recruitment domain (ASC) adaptor, and the procaspase-1 effector (*1*, *2*, *4*, *5*). Early studies revealed that germline mutations and hyperactivity of NLRP3 are associated with rare hereditary autoinflammatory diseases in humans (*6*–*8*). NLRP3 has also now been implicated in the development of many common diseases including Parkinson's disease, Alzheimer's disease, cardiovascular diseases, and age-related metabolic complications (*1*, *6*–*9*).

In macrophages, activation of the NLRP3 inflammasome involves two steps. In the first step, known as priming, Toll-like receptors (TLRs) on the cell surface recognize pathogen-associated molecular patterns or damage-associated molecular patterns (DAMPs). This leads to enhanced production of inflammasome proteins, including NLRP3 and the precursor of proinflammatory cytokine interleukin-1β (IL-1β) (*1*, *2*, *4*, *5*). In the second step, known as activation, various molecules including extracellular adenosine 5′-triphosphate (ATP) or bacterial toxins like nigericin induce cellular K^+ efflux and NLRP3 activation (*1*, *2*, *4*, *5*). Active NLRP3 recruits ASC, which is thought to polymerize and thereby cause caspase-1 processing via proximity-induced self-cleavage (*1*–*3*, *5*, *10*). Active caspase-1 cleaves the precursors of IL-1β and IL-18, leading to their maturation (*11*). Active caspase-1 also cleaves the pore-forming protein gasdermin D (GSDMD), which then forms pores in cytoplasmic membranes that release the processed cytokines and induce pyroptosis (*12*).

By fluorescence microscopy, the NLRP3 inflammasome is seen as a single speck within each cell (*13*–*15*). Some of us (Magupalli *et al.*) and others showed previously that this single speck contains the caspase-1 holoenzyme and colocalizes with the microtubule-organizing center (MTOC) (*9*, *14*, *16*). Additional studies supported the MTOC localization of the NLRP3 inflammasome as the NIMA-related kinase 7 (NEK7) implicated in NLRP3 activation (*17*–*19*) is a centrosomal kinase important for mitosis, and a recent study demonstrated that NLRP3 inflammasome activation compromises centrosome integrity (*20*). Emerging evidence also reveals that NLRP3 inflammasome activation and cell division are mutually exclusive, again hinting that the MTOC is actively involved (*18*). Furthermore, many other organelles have been associated with NLRP3 activation, including mitochondrial damage (*21*–*23*), Golgi cisternae dispersion, and endosomal trafficking disruption (*24*, *25*).

Many in vitro structures of purified components and reconstituted subassemblies are already available, including cryo–electron microscopy (cryo-EM) structures of inactive, monomeric NLRP3 in complex with NEK7 (*26*, *27*), oligomeric NLRP3 in cage form (*27*–*30*), active NLRP3 in disc form in complex with NEK7 and ASC (*10*), and pyrin domain and caspase-recruitment domain (CARD) filaments of ASC (*31*–*33*). A recent in situ cryo–electron tomography (cryo-ET) study in ASC-overexpressing mouse immortalized bone marrow–derived macrophages (iBMDMs) (*34*) revealed networks of ASC filaments in both labeled and unlabeled cells away from the MTOC (*31*). However, because inflammasome specks form at the MTOC only in wild-type but not ASC-overexpressing iBMDMs (*14*), this cryo-ET study leaves open key questions regarding organelle-dependent characteristics of NLRP3 inflammasome activation.

Cryo–focused ion beam (cryo-FIB) milling and cryo-ET have become powerful techniques to visualize protein complexes in their near-native state in situ to macromolecular resolution (*35*, *36*), but

[1]Division of Chemistry and Chemical Engineering, California Institute of Technology, Pasadena, CA 91125, USA. [2]Division of CryoEM and Bioimaging, SSRL, SLAC National Accelerator Laboratory, Menlo Park, CA 94025, USA. [3]Department of Biological Chemistry and Molecular Pharmacology, Harvard Medical School, Boston, MA 02446, USA. [4]Program in Cellular and Molecular Medicine, Boston Children's Hospital, Boston, MA 02446, USA. [5]Department of Chemistry and Biochemistry, Brigham Young University, Provo, UT 84602, USA.
*Corresponding author. Email: pdahlb@stanford.edu (P.D.D.); wu@crystal.harvard.edu (H.W.); grant_jensen@byu.edu (G.J.J.)
†Present address: Institute of Precision Medicine, The First Affiliated Hospital, Sun Yat-Sen University, Guangzhou 510275, Guangdong, China.
‡Present address: Laboratory of Molecular and Mechanistic Cell Signaling, Lindsley F. Kimball Research Institute, New York Blood Center, 610 Midland Avenue, Rye, NY 10580, USA.

targeting specific objects is challenging. Previous studies have used fluorescent markers to target certain organelles and large protein aggregates (*31*, *36*, *37*). However, guidance of the milling along the axis of the light microscope remains challenging because of the limited resolution in the axial direction, registration errors between the light microscopy and FIB-milling positions, and warping of the sample during milling. These challenges persist even when the light microscope is integrated into the FIB-SEM vacuum chamber when the optical imaging position and the milling position are still separate. As a result, small targets are nearly always lost during milling (*31*, *38*–*40*). Here, we used a tri-coincident cryo–FIB-SEM fluorescence instrument (*41*) called the ENZEL to overcome these challenges. The ENZEL allows real-time simultaneous fluorescence and cryo-FIB imaging to precisely guide the milling. Using ENZEL for milling followed by cryo-ET, we directly visualized NLRP3 inflammasomes in situ at the MTOC in human macrophages, capturing various stages of activation across 82 cryo-tomograms. The images revealed insights into the NLRP3 structure and organelle alterations that occur during inflammation.

RESULTS

Cell lines and NLRP3 inflammasome activation

We constructed a human THP-1 monocytic cell line with a fluorescent marker, mScarlet, fused to NLRP3, referred to as mSL-NLRP3 cells (fig. S1A). This was done in a cell line in which endogenous NLRP3 had been knocked out (NLRP3 KO). THP-1 monocytic cells were then differentiated into macrophages and became adherent. This mSL-NLRP3 macrophage cell line recapitulated all the hallmark behaviors of wild-type inflammasome activation: After priming with lipopolysaccharides (LPSs) and stimulating with nigericin [a potassium ionophore frequently used to activate NLRP3; (*42*, *43*)], we observed ASC speck formation, GSDMD processing, and cell death as shown by lactate dehydrogenase (LDH) release (fig. S1, B to D). These effects were seen in wild-type and mSL-NLRP3 cells, but not in the parent NLRP3-KO cells, confirming the dependence of the processes on NLRP3 (fig. S1, B to D). We also added SiR-tubulin to mark the MTOC (*44*). In live cells, we observed no NLRP3 punctum formation before priming (fig. S1E). Addition of LPSs, which activate TLR4, led to the formation of a diffuse NLRP3 signal covering the MTOC (fig. S1E). We then added nigericin and observed a NLRP3 fluorescence signal colocalized with the MTOC, as seen in other inflammasome studies (fig. S1, E and I) (*9*, *14*, *16*).

Although constructing stable THP-1 cell lines expressing green fluorescent protein family fusion constructs has been widely applied to study the NLRP3 inflammasome pathway (*14*, *28*, *31*, *45*), as a control, we tested whether NLRP3 punctum formation was an artifact of aggregated mScarlet by generating a THP-1 cell line expressing mScarlet fluorescent protein only. We differentiated this cell line and followed the same activation protocol that we applied to the mSL-NLRP3 cells. In live cells, we found no puncta before or after nigericin treatment: mScarlet fluorescence remained distributed evenly across the cell volume in all experimental conditions (fig. S1F). As expected, SiR-tubulin fluorescence appeared as a bright single punctum in cells, similar to the phenotype observed in mSL-NLRP3 cells (fig. S1F). Previous inflammasome studies also reported that extracellular ATP behaved as a DAMP, signaling the P2X purinoceptor 7 and inducing potassium efflux (*46*–*51*). We observed that extracellular ATP also led to formation of puncta at the MTOC (fig. S1, G and I). Next, we tested the potassium-independent activation pathway driven by imiquimod, a TLR7 ligand (*45*, *52*, *53*). NLRP3 puncta again formed at the MTOC (fig. S1, G and I) (*45*, *52*, *54*).

We then asked the question whether NLRP3 inflammasome punctum formation in mSL-NLRP3 cells requires ASC. When cells were treated with MCC950, which has no effect on inflammasome priming or potassium efflux but directly inhibits NLRP3 activation by stabilizing the inactive conformation (*55*, *56*), NLRP3 only accumulated as a diffuse cloud covering the MTOC (fig. S1H). When cells were treated with the caspase-1 inhibitor z-VAD-FMK (*57*–*59*), NLRP3 puncta were again observed at the MTOC (fig. S1, H and I); despite testing these various conditions, we never observed NLRP3 speck formation far away (micron or more) from the MTOC as previously reported (*31*). Together, these results confirm that the NLRP3 puncta that we observed at the MTOC are not artifacts of tagging and behave as expected after inflammasome activation by potassium-dependent and potassium-independent pathways.

Uncovering NLRP3 inflammasomes for cryo-ET imaging

mSL-NLRP3 cells were grown on electron microscopy (EM) grids, primed with LPS, and activated with nigericin. Cells were plunge frozen at various time points before and after priming and activation. As observed previously on glass slides, addition of nigericin to LPS-primed cells grown on EM grids caused mScarlet fluorescence to condense into a single bright punctum colocalized with the MTOC (figs. S1E and S2A). Before inflammasomes could be imaged by cryo-ET, they had to be uncovered and preserved in lamellae just a few hundred nanometers thick. This is technically challenging because the volume retained in a lamella represents less than 1% of the original cell, and it is difficult to locate targets precisely or prevent them from moving during milling (*60*–*64*). Moreover, because each cell contains only a single inflammasome punctum per cell, targeting it precisely for milling becomes even more challenging. To overcome these obstacles, we used a tri-coincident cryo–FM-FIB-SEM system called the ENZEL, which allows simultaneous fluorescence measurement and FIB milling (*41*). After milling, final fluorescence images of the lamellae were obtained, and the locations of MTOC-associated fluorescence were noted. In every lamella imaged by cryo-ET in this study that contained a NLRP3 punctum, it colocalized with the MTOC (fig. S2B). Lamellae were transferred into a Titan Krios transmission electron microscope, and tilt-series were recorded at the locations of MTOC fluorescence. The final fluorescence images were overlaid on the cryo-tomograms. The brightest SiR-tubulin fluorescence correlated precisely with centrioles in the cryo-tomograms, unambiguously marking the MTOC (Fig. 1, A and B). Centrioles were found in 60 of the 82 resulting cryo-tomograms, and nine exhibited both centrioles (fig. S2, C to E), a marked increase in targeting success compared with that in previous work without the ENZEL (*65*, *66*).

NLRP3 accumulates into a condensate at the MTOC

In nigericin-stimulated mSL-NLRP3 cells, but not in untreated or LPS-primed cells, an electron-dense region containing irregular, patch-like densities and small vesicles was seen between and around the centrioles, expanding to ~2 μm in diameter (Figs. 1, C and D, and 2, H to J; fig. S3A; and movies S1 to S5). These patch-like densities were heterogeneous in size and shape, ranging from 30 to 200 nm (fig. S3B), whereas the small vesicles were relatively homogenous (Figs. 1, C and D, and 2, C, D, H, and I; and movies S3 and S4),

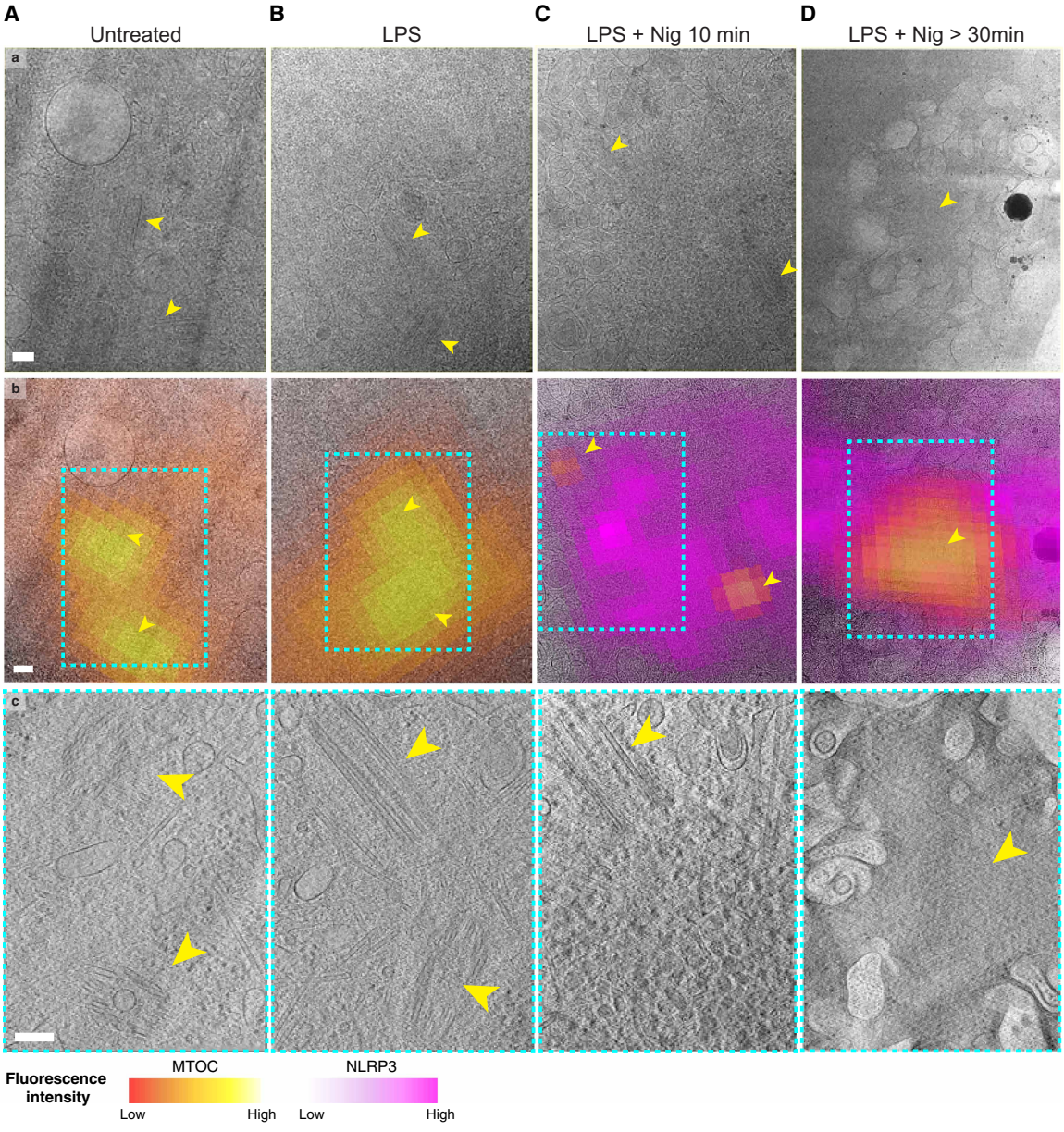

Fig. 1. Progression of NLRP3 inflammasome activation. (**A** to **D**) Representative tomographic slices at increasing magnification showing the MTOC and the formation of the NLRP3 inflammasome condensate, ordered chronologically: (a) cryo-ET atlas, (b) fluorescence-correlated cryo-ET atlas overlaid with (a), and (c) representative tomographic slices obtained from the designated imaging area indicated by cyan dashed lines in (b). The MTOC and NLRP3 inflammasome are colored yellow and magenta, respectively, on the basis of the fluorescence intensity profile. Two centrioles from the MTOC are indicated by yellow arrowheads. Arrowhead positions were determined from (b) and superimposed onto (a) and (c), respectively. Number of events at each stage: untreated, $n = 12$; LPS, $n = 10$; LPS + Nig 10 to 20 min, $n = 10$; LPS + Nig > 30 min, $n = 3$. Scale bars, 200 nm for all panels.

with an average size of ~50 nm. The mScarlet fluorescence correlated precisely with this electron-dense region, identifying it as rich in NLRP3, while SiR-tubulin fluorescence marked the centrioles (Figs. 1, C and D, and 2, C to E and H to J; and fig. S3A). We also collected cryo-tomograms of lamellae slightly above or below the MTOC, with mScarlet fluorescence only but without SiR-tubulin fluorescence (fig. S3A and movie S6). At these positions, we again observed patch-like densities and 50-nm vesicles with a similar spatial distribution, suggesting that these densities do not vary with distance from the MTOC.

Before nigericin stimulation, the regions surrounding the MTOC were populated with ribosomes. Following nigericin treatment, ribosomes were excluded (Fig. 2). Thus, the NLRP3 inflammasome punctum is a patchy, electron-dense, ribosome-excluding condensate, consistent with features observed in other described cellular condensates (*67*, *68*). Over time, the number of small vesicles as well as microtubule nucleation sites decreased, further indicating that the condensate progressively excluded other cellular structures (Fig. 3A). No extended filaments besides microtubules were observed. At later time points after nigericin activation (>30 min), fewer small patches

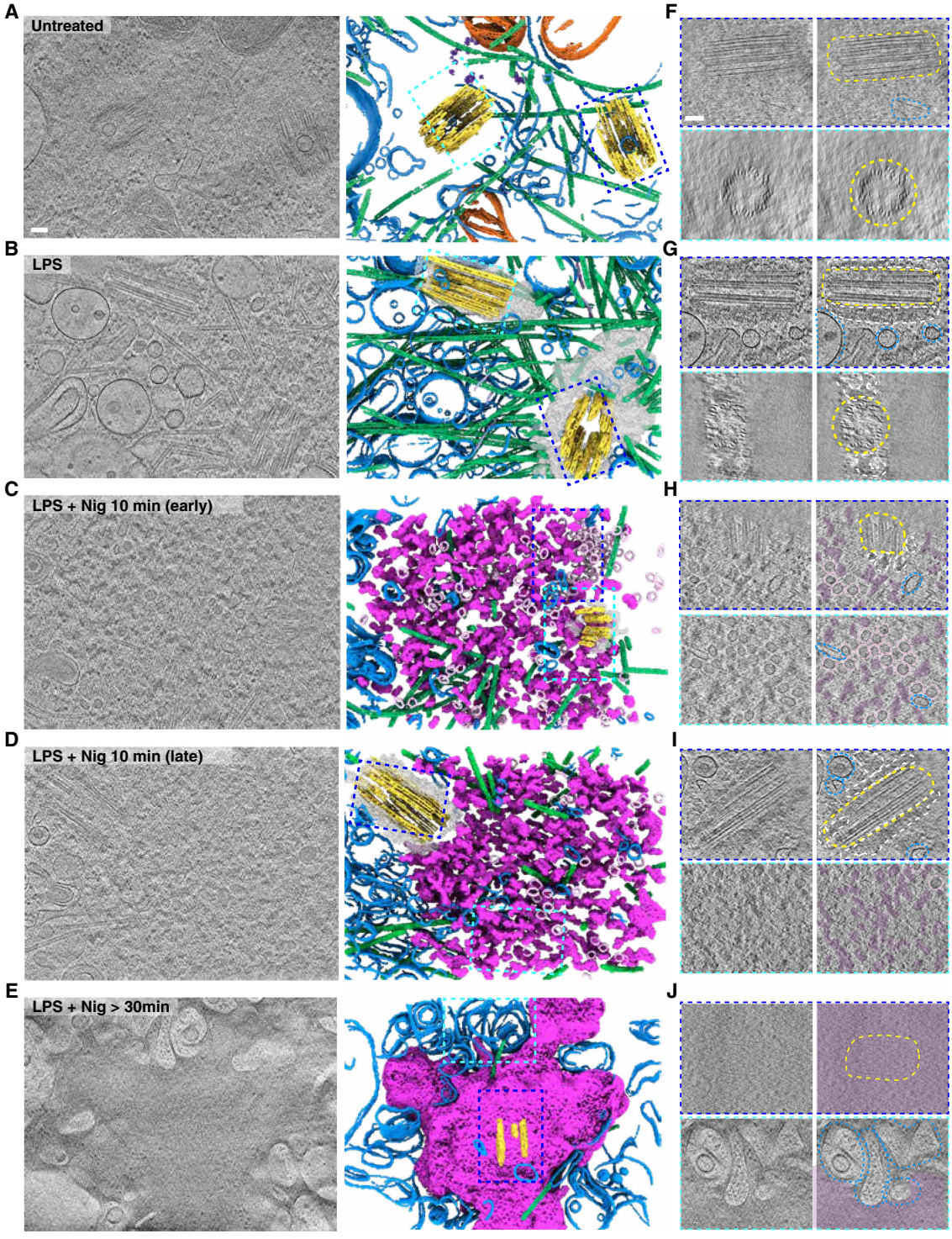

Fig. 2. NLRP3 inflammasome activation leads to formation of condensate at the MTOC. (**A** to **E**) Representative tomographic slices and segmented models illustrating NLRP3 inflammasome activation (MTOC, yellow; microtubules, green; NLRP3-associated vesicles, light pink; NLRP3 condensate, magenta; membrane, blue; mitochondria, orange; ribosomes, purple; scale bars, 100 nm). Tomographic slices in [(A), (D), and (E)] were obtained from cells shown in Fig. 1. (**F** to **J**) Enlarged and rotated views of the areas immediately surrounding the centriole marked by the dashed boxes in [(A) to (E)].

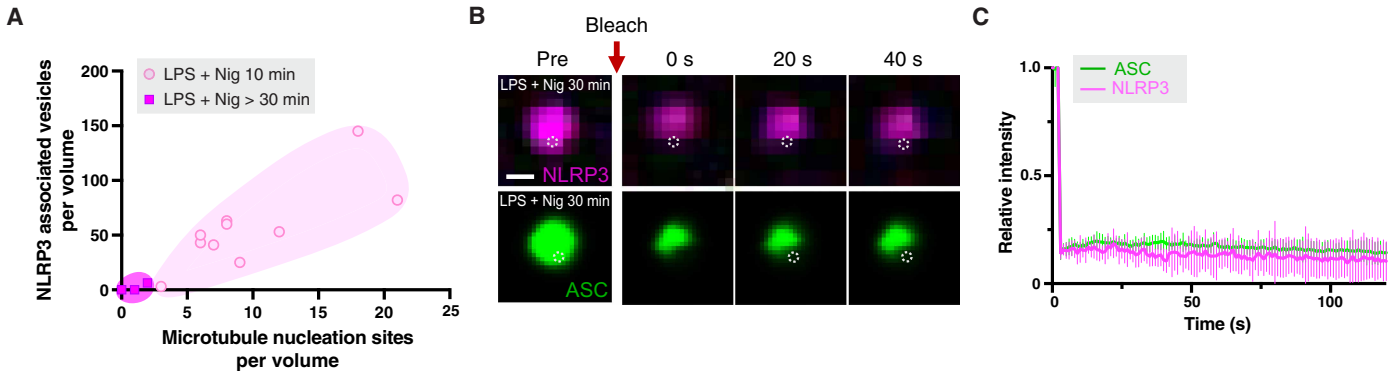

Fig. 3. NLRP3 inflammasome becomes an immobilized solid condensate. (**A**) Correlation analysis of number of the NLRP3-associated vesicles and the number of microtubule nucleation sites within the NLRP3 condensate. Each data point represents one cell. Individual cells treated with LPS + Nig 10 min are indicated as light pink circles; cells treated with LPS + Nig > 30 min are marked as magenta squares. The area shaded in light pink includes all cells treated with LPS + Nig 10 min; area shaded in magenta includes all cells treated with LPS + Nig > 30 min. (**B** and **C**) Tracking of NLRP3 mobility by fluorescence recovery after photobleaching (FRAP). Bleached areas indicated by white dashed circle (scale bar, 1 μm).

were seen, replaced instead by a large, more uniform dense condensate (Figs. 1D and 2, E and J; and movie S5).

To investigate the biophysical properties of the late-stage inflammasome condensate, we performed fluorescence recovery after photobleaching (FRAP) experiments using mSL-NLRP3 cells coexpressing mNeonGreen-tagged ASC. Neither NLRP3 nor ASC in the inflammasome speck showed FRAP (Fig. 3, B and C), suggesting that the condensate had transitioned into a stable, solid-like state.

Inflammasome formation perturbs the MTOC conformation

In our tomographic reconstructions, each centriole appeared as a ring of nine triplets of microtubules of 500 to 700 nm in length and ~250 nm in diameter (Fig. 2, F, G, and I), consistent with previous studies (*65*, *69*–*71*). In untreated cells, the two centrioles were found to lie perpendicular to each other, spaced an average of 500 nm apart (Fig. 4A), also consistent with other studies (*72*). Because these distances are close to the diffraction limit of our imaging system, under these conditions, the two centrioles' fluorescence signal partially overlapped but had distinct maxima (Fig. 1, A and B).

Ten minutes after nigericin stimulation, the two centrioles were observed ~2 μm away from each other (Fig. 4A) and nearly parallel (Fig. 1C). Notably, before cryo-FIB milling, the SiR (tubulin) fluorescence appeared as a single punctum in the cryo–light microscope, but, after milling, each centriole could be resolved (fig. S2C). Centriole separation was also observed in a portion of live cells after 20 and 50 min of nigericin stimulation (Fig. 4, B and C). The intensity profile of the MTOC channel clearly showed two distinguishable peaks with the mScarlet channel covering both peaks, suggesting that the two centrioles are pushed apart by the growing NLRP3 condensate (Fig. 4B). Because centrioles were not always discernible in the cryo-tomograms within the late-stage condensates 30 or more min after nigericin treatment, we could not measure centriole separation at this time point in the cryo-ET data. Instead, we showed by fluorescence in live cells that the centriole separation persists as activation proceeds (Fig. 4, B and C).

The distance between centrioles is known to vary as the cell cycle progresses, with centrioles typically separated by less than 2 μm during the G_1-S phase and by more than 2 μm in the G_2-M phase. Additionally, centriole duplication occurs during the S phase and continues into the G_2-M phase, beginning with the elongation of procentrioles (*73*–*79*). Although we consistently observed separated centrioles in our cells after inflammasome activation, no elongated procentrioles were seen. This absence is unlikely to be due to loss during cryo-FIB milling, as nascent daughter centrioles are tightly associated with their mother centrioles (~50 nm) (*80*). None of the centriole pairs that we imaged, either by cryo-ET or fluorescence, were separated by more than 2 μm, suggesting that the cells were in the G_1-S phase (Fig. 4, A to C). Thus, these findings suggest that NLRP3 inflammasome activation alters or arrests cell-cycle progression, maintaining cells in a G_1-S–like state (*18*).

The pericentriolar material (PCM) has been recognized as a phase-separated compartment closely associated with the centrioles, serving as a scaffold for microtubule nucleation (*81*, *82*). Intriguingly, however, previous in situ cryo-ET studies of the mammalian MTOC and *Caenorhabditis elegans* MTOCs revealed PCM as a low-contrast, seemingly "empty space" that excluded most cellular components (*65*, *66*). While we could not discern PCM in the cryo-tomograms of untreated cells, priming with LPS resulted in the appearance of dark amorphous densities with well-defined boundaries, tightly associated with the centrioles (Fig. 2, B and G, and fig. S3A). As a similarly dark amorphous material was identified as PCM in a previous report (*65*), we interpreted these densities to be PCM. In untreated cells, we observed only a few microtubule nucleation sites in close proximity to the centrioles, but, in LPS-primed cells, there were many more located within the PCM (Fig. 4, D and E). Microtubule nucleation sites were identified by conically shaped γ-tubulin ring complexes at the tip (Fig. 4E) (*83*–*85*). Recruitment of PCM and enhanced microtubule nucleation are both recognized hallmarks of interphase centrosome maturation (*86*).

Inflammasome activation induces Golgi cisternae expansion and disruption

In untreated cells, we observed Golgi stacks with 20- to 30-nm-thick cisternae, similar to what has been reported in previous studies (Fig. 5, A and B) (*87*). Following LPS priming, the diameter of cisternae expanded to 80 to 100 nm (Fig. 5, A and B), an effect previously reported to reflect increased cargo loading (*88*, *89*). To investigate Golgi structure with a wider field of view than possible with

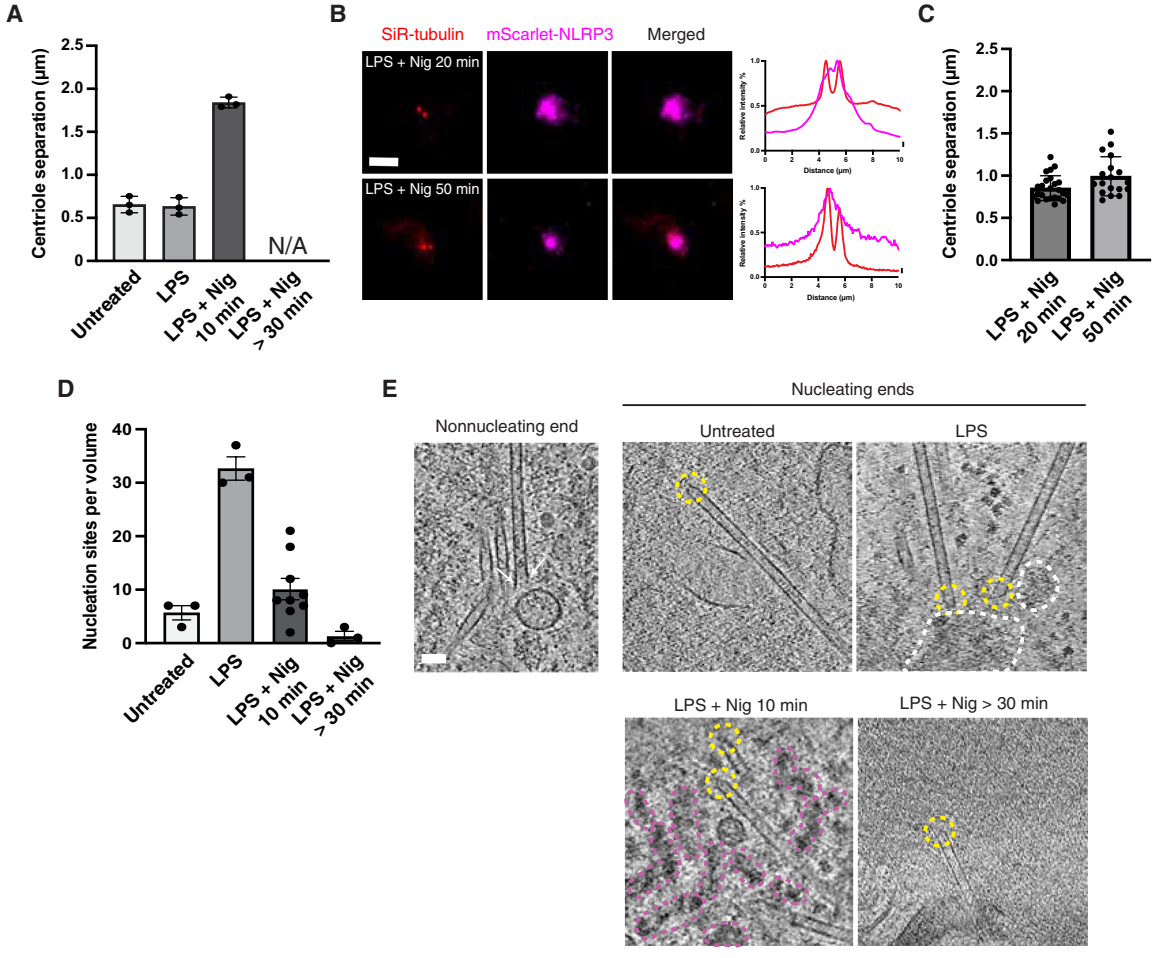

Fig. 4. NLRP3 inflammasome activation alters MTOC conformation. (**A**) Distance of centriole separation measured by cryo-ET in response to NLRP3 inflammasome activation [one-way analysis of variance (ANOVA), $P < 0.0001$]. (**B**) Live-cell imaging of mSL-NLRP3 cells after NLRP3 inflammasome activation showing separated centrioles (scale bar, 5 μm). Fluorescence intensity profiles of puncta are shown in the last panel of each row. (**C**) Distance of centriole separation by live-cell imaging in response to NLRP3 inflammasome activation (*t* test, $P = 0.02$). (**D**) Quantification of the number of nucleation sites in the presence of a complete MTOC. Each data point represents one cell (one-way ANOVA, $P < 0.0001$). (**E**) Representative tomographic slices showing nonnucleating ends and MT nucleation sites at different conditions. The nonnucleating end is marked by two white arrows, and nucleation sites are circled in yellow; PCM and NLRP3 condensate are marked by white and magenta dotted circles, respectively (scale bar, 50 nm).

cryo-ET, we stably expressed TGN38-mNeonGreen and recorded fluorescence images. The area containing TGN38 also appeared to be larger in LPS-primed cells compared with untreated cells, supporting Golgi expansion (Fig. 5C). This supports the hypothesis that LPS priming alone is sufficient to drive the reported increase in NLRP3 abundance in the Golgi (*90*).

In LPS-primed cells we also noticed clusters of ~50-nm vesicles close to the expanded Golgi (Fig. 6A, fig. S4A, and movie S7). The vesicle concentration correlated with mScarlet fluorescence intensity, indicating the presence of concentrated NLRP3 (fig. S5). Similar small vesicles were not observed in untreated cells or regions outside NLRP3 fluorescence (Fig. 6A). The presence of these vesicles in LPS-primed human THP-1 cells is consistent with the recent finding that NLRP3 is immobilized on the Golgi before addition of nigericin (*91*). In nigericin-activated cells, we saw 50-nm vesicles in larger numbers, but we could not detect any special spatial correlation between the clusters of vesicles and mScarlet fluorescence because the fluorescence signal was uniformly high across the entire area due to the growth of the condensate (fig. S5). Sectioning through the vesicle subtomograms revealed densities inside the vesicles, but no apparent regular order (fig. S4B). Because NLRP3 cage structures, which have been implicated as the entities recruited to the Golgi (*28*), have two opposing PI4P-binding surfaces that may curve membranes to promote vesiculation, it is possible that the associated densities are cages. Attempts to perform subtomogram averaging the densities did not yield meaningful results, likely owing to the limited number of particles within a highly heterogeneous population.

After nigericin stimulation, little or no intact Golgi structure was seen (Fig. 5A). Instead, we observed diverse irregularly shaped membrane structures, which may have been cisternae unstacking and morphing away from their original shape (Fig. 5A). When THP-1 cells stably expressing TGN38-mNeonGreen were imaged, the TGN38 fluorescence appeared as dispersed speckles after nigericin stimulation (Fig. 5C), consistent with the cryo-ET data. We hypothesize that the 50-nm vesicles originate from Golgi cisternae during its dispersion (*28*, *92*) and serve to transport NLRP3 to the

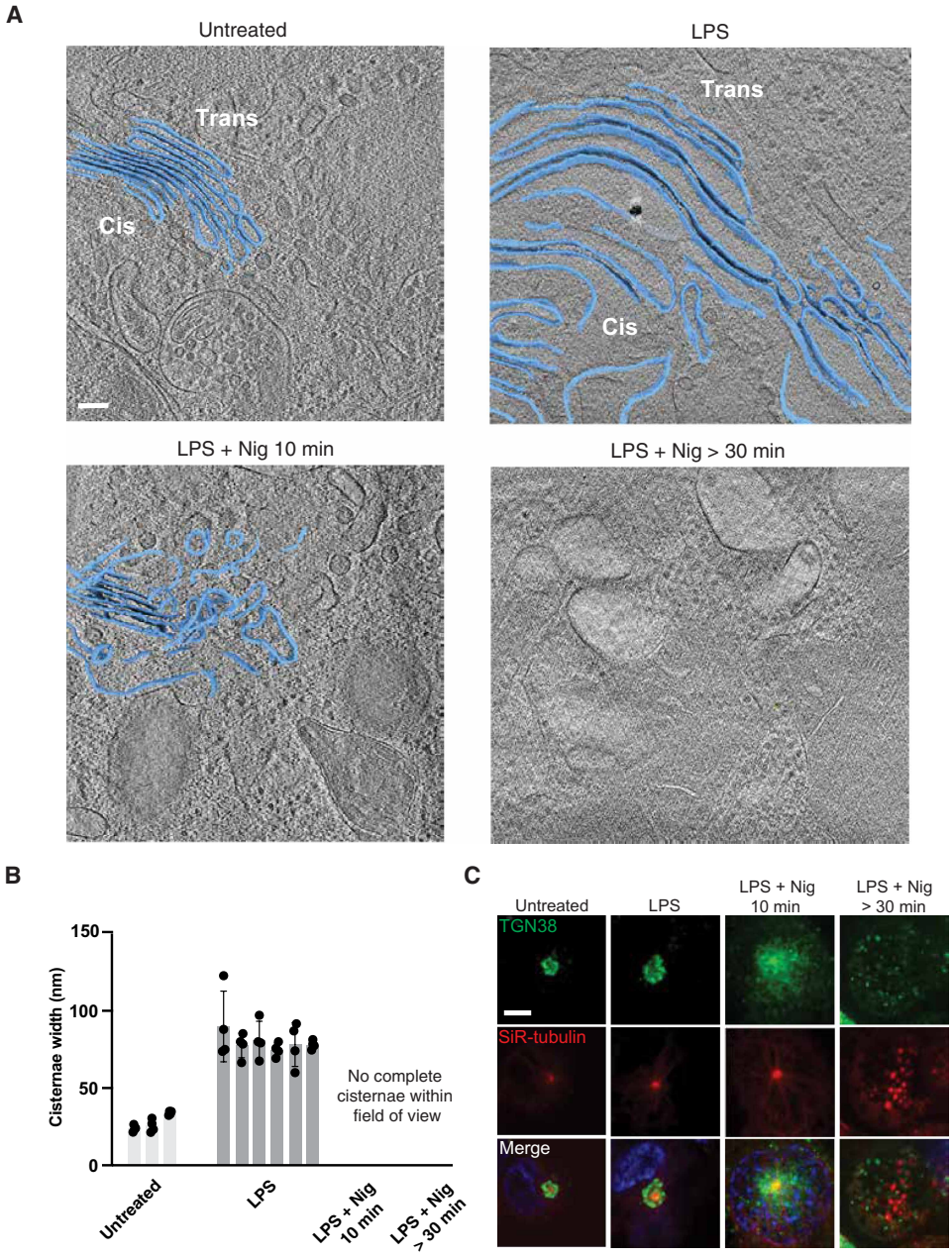

Fig. 5. Nigericin stimulation disrupts Golgi integrity. (**A**) Tomographic slices with segmented Golgi cisternae (Golgi cisternae, blue; $z = 10$; scale bar, 100 nm). The face of the Golgi was assigned on the basis of relative distance to the nucleus on lamellae, with the Cis face closer to the nucleus. (**B**) Quantification of cisternae spacing in response to LPS. Each bar represents three distance measurements for each Golgi structure. All cells were from different passages and different grids (untreated, $n = 3$; LPS, $n = 6$; one-way ANOVA, $P < 0.0001$). (**C**) Fluorescence imaging of TGN38-mNeonGreen and SiR-tubulin during NLRP3 inflammasome activation (scale bar, 5 μm). Nucleus is shown in blue.

MTOC (Fig. 6, A and B), although whether NLRP3 is on the inside or outside of the vesicles remains unclear. Consistent with this hypothesis, some vesicles were nonspherical or even flattened, which might be expected for different stages of content release (Fig. 6B).

In mouse macrophages, NLRP3 has been shown to interact with microtubules and intermediate filaments, and inflammasome activation depends on histone deacetylase 6 (HDAC6)–mediated microtubule transport (*14*, *16*, *93*, *94*). Unexpectedly, then, we found very few 50-nm vesicles in close contact with microtubule networks or intermediate filaments (fig. S4C). We therefore tested in our human cell line whether inflammasome activation was also dependent on HDAC6-mediated microtubule transport. In agreement with a previous report (*90*) and unlike mouse iBMDMs (*14*, *17*–*19*), we found NLRP3 punctum formation in both wild-type and mSL-NLRP3 human THP-1 cells to be independent of microtubule transport, as shown by insensitivity to the microtubule disrupter colchicine and

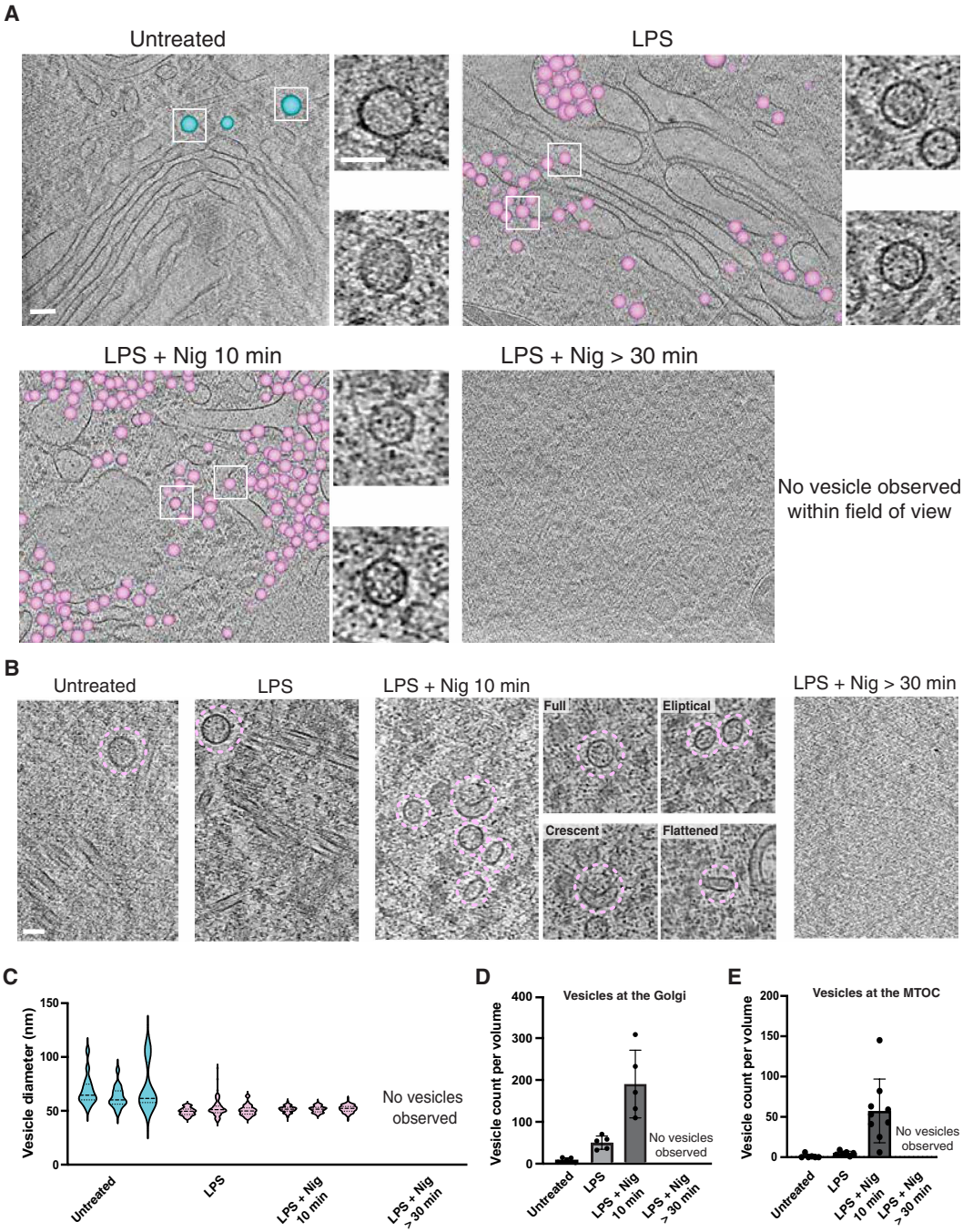

Fig. 6. NLRP3-associated vesicles traffic to the MTOC independently of microtubule transport. (**A**) Overlaid tomographic model on segmented slices showing vesicles observed at the Golgi (vesicles observed before priming and NLRP3 inflammasome activation, cyan; vesicles observed after priming and NLRP3 inflammasome activation, light pink; scale bar, 100 nm). Enlarged views of representative vesicles observed under each condition are indicated by white boxes (scale bar, 50 nm). (**B**) Representative tomographic slices showing vesicles near the MTOC before and after NLRP3 inflammasome condensate formation ($z = 10$). Vesicles are circled in light pink. (**C**) Quantification of vesicle diameters in response to NLRP3 inflammasome activation. Each violin plot represents one cell (one-way ANOVA, $P < 0.0001$). (**D**) Quantification of vesicle numbers observed near the Golgi in response to NLRP3 inflammasome (one-way ANOVA, $P < 0.0001$). Each data point represents one cell. (**E**) Quantification of number of vesicles present at the MTOC under different conditions. Each data point represents one cell (one-way ANOVA, $P < 0.0001$).

the HDAC6 inhibitor tubacin (fig. S1, C and D). This microtubule and NEK7 independence in human THP-1 cells is particularly intriguing as the human inflammasome is still formed at the MTOC.

We also obtained cryo-tomograms of a few LPS-primed cells in which both the MTOC and Golgi stacks were retained in the final lamellae. In these cases, the swollen Golgi stacks appeared as close as 200 nm from a centriole (fig. S4A). By contrast, in untreated mSL-NLRP3 cells, the MTOC and Golgi were never seen together in the same cryo-tomogram, indicating that they are more than a few microns apart (the field of view of one cryo-tomogram). These findings suggest that priming-induced cisternal expansion brings Golgi structures appear closer to the MTOC.

Mitochondria are recruited to inflammasomes and appear damaged

Mitochondria have been reported to play a role in the NLRP3 inflammasome activation pathway (*23*, *95*–*97*). Liu *et al.* (*31*) showed abnormal cristae structures in nigericin-activated, ASC-overexpressing mouse iBMDMs. We observed a plethora of mitochondrial morphologies in untreated, LPS-primed, and early nigericin-activated (10 min) mSL-NLRP3 cells, predominantly displaying intact outer membranes and evenly distributed cristae, with rare cases showing loss of cristae or irregularly shaped cristae (fig. S6A).

However, the number of mitochondria within 5 μm of the MTOC and NLRP3 condensate increased markedly after 10 min of nigericin activation (Fig. 7). Cells treated with nigericin for more than 30 min revealed much larger mitochondria with reduced cristae (fig. S6A), an indication of damage (*98*). Mitochondria were seen in clusters, and some appeared to be fusing (Fig. 7B and fig. S6B). The formation of mitochondrial clusters has been reported in cells overexpressing the mitochondrial fusion protein Mfn2, a protein known to induce caspase-mediated apoptosis (*99*, *100*). Increased mitochondrial clustering and fusion have also been observed in cells with elevated levels of reactive oxygen species (ROS) (*101*, *102*). As GSDMD-mediated mitochondrial damage has been shown to induce ROS (*103*, *104*), we speculate that the mitochondrial clustering and fusion that we observed was caused by similar pathways.

NLRP3 inflammasome is a target of selective autophagy

After 10 min of nigericin activation, we observed accumulation of multiple, heterogeneous membrane structures at the periphery of the NLRP3 condensate (Figs. 1, C and D, and 2, C to E; and fig. S7A). Building on our previous findings that inflammasome puncta colocalize with the autophagy marker LC3b (*14*), we confirmed that NLRP3 fluorescence again colocalized with LC3b in mSL-NLRP3 cells, indicating that at least some of the associated membrane structures were autophagic (fig. S7, A to C). Notably, at the interface between the NLRP3 condensate and the autophagic site, we observed membrane structures actively intruding into the condensate (fig. S7A), suggesting localized autophagy activity. Within the condensate, phagophore-like structures, resembling those reported in prior studies (*105*, *106*), were also detected, further supporting the hypothesis that the inflammasome is a target of autophagy.

Mitochondria were also observed in direct contact with autophagosome-like structures surrounding the NLRP3 condensate, implicating their potential involvement in this process (fig. S6, A and B). Multilayered membrane structures tightly associated with the inflammasome condensate were observed after 30 min of nigericin (fig. S7D). At this stage, membrane structures appeared to have fewer internal features compared with earlier time points (fig. S7, B and D). Signs of membrane intrusion and internal phagophore formation persisted (fig. S7D).

The inflammasomes were enveloped by multiple layers of heterogeneous membrane structures reminiscent of the previous reports of autophagic membranes surrounding p62-positive gels (*107*), rather than classical, double-layered, membrane-enclosed autophagosomes (*108*, *109*). Inflammasomes may be recognized by p62, a direct binding partner of LC3b known to mediate selective autophagic clearance of phase-separated condensates (*107*, *110*–*112*).

DISCUSSION

Our data support the following model for NLRP3 inflammasome activation (Fig. 8). Upon LPS priming, the expression of NLRP3 and pro–IL-1β is up-regulated, accompanied by swelling of Golgi cisternae (*88*, *89*). These expanded Golgi structures give rise to 50-nm vesicles that are likely specialized and loaded with NLRP3 and potentially other inflammasome components. Concurrently, LPS priming leads to increased PCM density and microtubule nucleation, and the expanded Golgi lies closer to the MTOC. Upon nigericin stimulation, the swollen Golgi disperses, allowing 50-nm vesicles to diffuse a short distance to the MTOC, apparently without the need for active transport. There, the vesicles unload their cargo, which, together with ASC and caspase-1 form a condensate and trigger caspase-1 processing. Mitochondria are recruited and damaged, while autophagosomes accumulate and gradually envelop the inflammasome. The inflammasome condensate progressively solidifies, with no exchange of materials, and pyroptosis ensues.

Unexpectedly, in our cryo-tomograms, we did not detect regular, ordered structures within the early patches or mature condensates. This observation rules out the presence of long, extended polymeric ASC or caspase-1 filaments, although it does not exclude smaller complexes, such as full or partial inflammasome discs or short ASC or caspase-1 filaments (*10*). The potential existence of smaller complexes is supported by the solid nature of the condensates for both NLRP3 and ASC in the inflammasome speck. Disc-like NLRP3 structures in recombinant samples were only discernable after extensive two-dimensional classification of hundreds of thousands of particles, far beyond the particle counts achievable by cryo-ET. In contrast, the previous cryo-ET study of mouse iBMDMs overexpressing ASC reported filamentous structures away from the MTOC (*31*). Because our cells showed all the hallmark downstream effects of inflammasome activation and because high ratios of ASC to NLRP3 are required for prominent ASC filamentous structures to form in reconstituted systems (*10*), we posit that extended filamentous structures are not necessary for NLRP3 inflammasome activation in cells. Instead, smaller assemblies such as partial discs must be sufficient to drive dimerization of the caspase domain of caspase-1 and proximity-induced enzymatic activation (*10*).

Several centrosomal kinases involved in mitotic regulation, such as Polo-like kinase 1 (PLK1), PLK4, and NEK7, have also been implicated in the regulation of inflammasome activation, indicating shared molecular pathways between cell-cycle progression and innate immune signaling (*17*, *26*, *113*–*117*). Our results provide insight into why inflammasome activation and normal cell division are mutually exclusive (*18*). We found that LPS priming led to increased PCM and microtubule nucleation, features of centrosome maturation. We speculate that condensate formation disrupts centriole

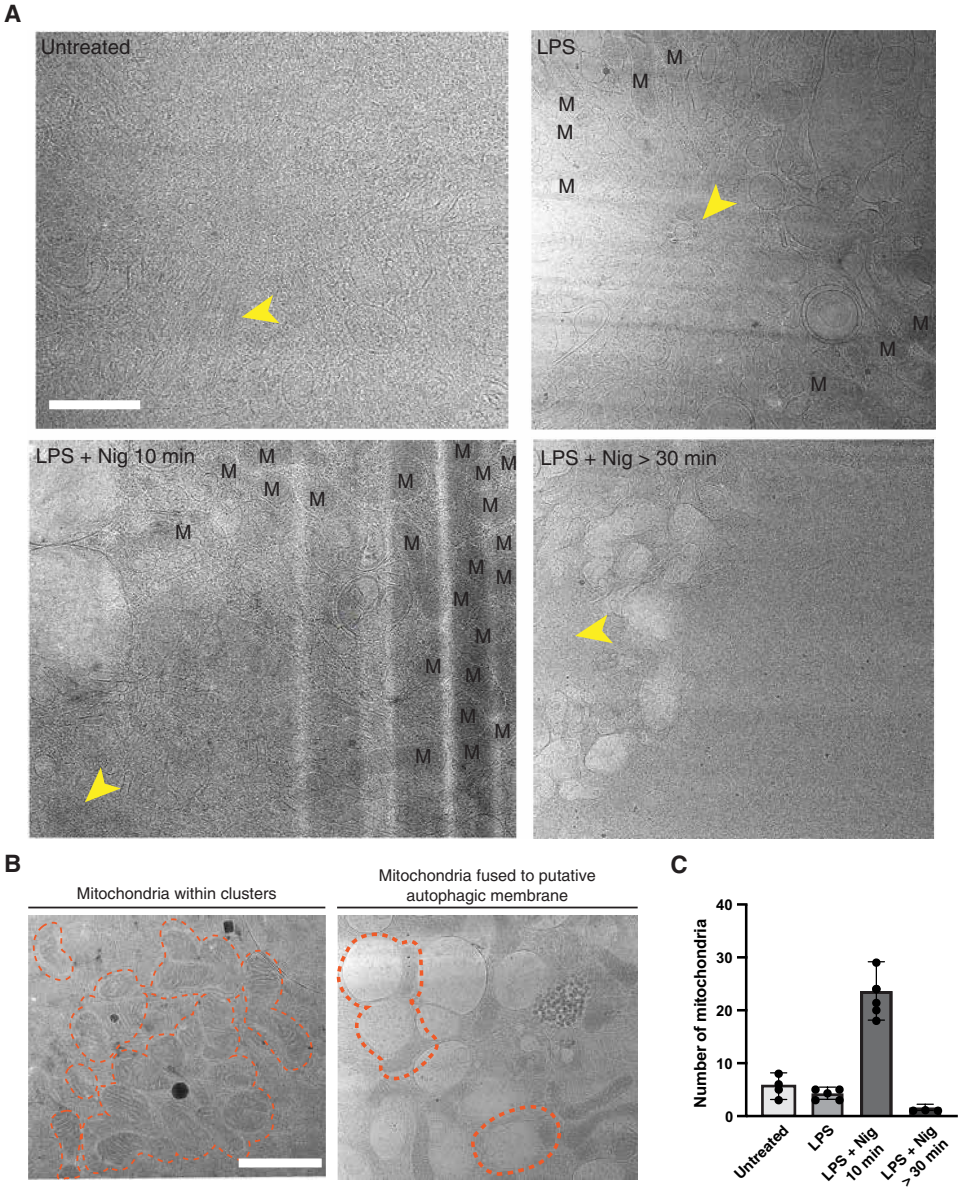

Fig. 7. NLRP3 inflammasome activation induces changes in mitochondria. (**A**) Representative atlas views of the MTOC and nearby mitochondria (scale bar, 1 μm). Centrioles are marked by yellow arrowheads, and mitochondria are denoted as "M." The same cell shown for LPS + Nig > 30 min is also displayed in Figs. 1D and 2E. (**B**) Representative examples of mitochondria clusters and mitochondria associated to putative autophagic membrane (dashed orange areas) after 10 min of nigericin treatment (scale bar, 100 nm). (**C**) Quantification of the number of mitochondria present within 5 μm of the MTOC. Each data point represents one cell (one-way ANOVA, $P < 0.0001$).

positioning and impedes molecular diffusion in and around the PCM, inhibiting normal mitotic progression (*86*). These observations align with two recent findings: one showing that microtubule nucleation requires dynamic PCM (*82*) and another reporting loss of PCM as a consequence of NLRP3 inflammasome activation (*118*). Perhaps the increased PCM density and microtubule nucleation create a microenvironment that recruits NLRP3 vesicles and initiates condensate formation.

Numerous studies have shown that NEK7 is involved in both mitosis and NLRP3 inflammasome activation (*17*, *26*, *113*, *114*). NEK7 is a centrosomal kinase that regulates mitosis by facilitating microtubule nucleation and promoting centrosome enrichment (*114*). In recent years, it has also become evident that mechanisms of NLRP3 inflammasome activation differ between species (*17*–*19*, *90*). Notably, while mouse cells require NEK7 for NLRP3 activation and speck formation (*10*, *17*–*19*), primed human cells do not (*90*). In mouse macrophages, NEK7's role in NLRP3 inflammasome activation appears to rely on its scaffolding rather than its kinase activity.

Intracellular vesicle trafficking is a well-known process for the exchange of materials between membrane-enclosed organelles (*119*). Facilitated by motor proteins and cytoskeleton tracks, cargoes secured in vesicles can be transported long distances from one cellular compartment to another. However, much less is known about vesicle trafficking across short distances. One example is found at the synapse, where

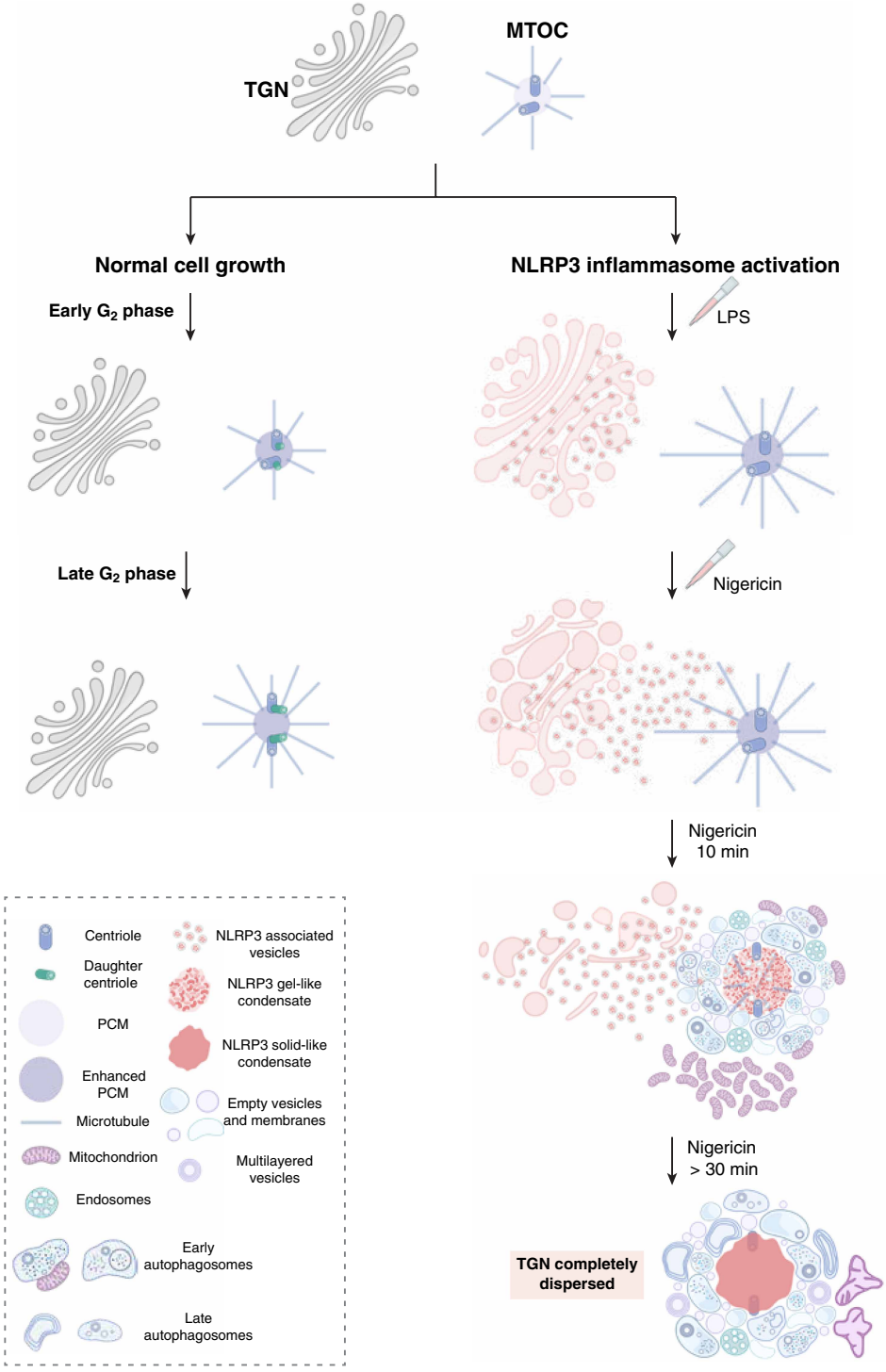

Fig. 8. Progression of NLRP3 inflammasome activation at the MTOC. Cartoon representations are annotated in the bottom left. The NLRP3-associated vesicles were modeled on the basis of reported structure (*28*). Created in BioRender. Wang, J. (2026) https://BioRender.com/caz6cqu.

presynaptic vesicles in the phase-separated reserve pool travel ~200 to 300 nm to reach the phase-separated active zone, without the need for active transport (*120*–*123*). Similarly, the NLRP3-associated vesicles observed in our study exhibit similar features comparable to presynaptic vesicles: Both are spherical, on average 50 nm in diameter, enriched at specific subcellular regions, and appear to diffuse short distances to a phase-separated compartment (*124*, *125*). Their uniform and small size may be optimized for short-distance diffusion rather than long-distance, motor-driven trafficking.

Biomolecular condensate formation by phase separation has now been implicated in numerous biological processes (*126*–*128*), including immunity. Condensates concentrate proteins and drive

rapid, switch-like signaling through threshold behavior (*129*–*133*). Some of us (Shen *et al.*) previously found that NLRP6, an inflammasome protein in the same family as NLRP3, contains intrinsically disordered regions and forms dynamic condensates when bound to viral dsRNA or bacterial lipoteichoic acid (*131*). The condensate can recruit the ASC adaptor, which, in turn, recruits caspase-1, leading to solidification of the condensate (*131*). Emerging evidence also showed that zDHHC7-mediated NLRP3 palmitoylation promotes its phase separation, thereby facilitating NLRP3 inflammasome activation (*134*, *135*). Notably, a recent in situ study of Apaf-1, which contains a CARD domain responsible for oligomerization into the apoptosome structure, also revealed meshwork-like structures, rather than the wheel-shaped assembly repeatedly observed by single-particle cryo-EM (*136*–*142*). Such differences highlight the importance of imaging structures in their native cellular environments. Further elucidation of these mechanisms could open up avenues for therapeutic strategies to dampen overactive immune pathways.

Our tri-coincident cryo–FIB-SEM fluorescence instrument allowed us to routinely uncover and preserve in lamella subdiffraction-limited fluorescent targets like centrioles and inflammasomes. The resolution of the fluorescence microscopy on the final polished lamella was even sufficient to show a pixel-by-pixel correlation between fluorescence intensity and the abundance of small vesicles, providing strong evidence that the vesicles contained NLRP3. By freezing cells at different time points, we were able to elucidate the entire inflammasome activation process. Technological advances continue to open opportunities for directly visualizing molecular complexes in situ by cryo-ET.

MATERIALS AND METHODS

Constructs and cloning

pLenti-CMV-Flag-mScarlet-NLRP3 was previously described (*28*). TGN38-mNeonGreen and mNeonGreen-ASC were cloned into the pHAGE-EF1α vector between Xba I and Nhe I sites using Gibson Assembly Master Mix [New England Biolabs, Inc. (NEB), catalog no. M5510].

Generation of stable cell lines

To produce lentiviral particles, human embryonic kidney 293T cells (80% confluence) in 10-cm dishes were cotransfected with 10 μg of pLenti-CMV-Flag-mScarlet-NLRP3, 10 μg of pHAGE-EF1α-TGN38-mNeonGreen, or 10 μg of pHAGE-EF1α-mNeonGreen-ASC and packaging plasmids 7.5 μg of psPAX2 and 3 μg of pMD2.G (Addgene, plasmid nos. 12260 and 12259). Twelve hours after transfection, the medium were removed and replenished with 8 ml of fresh medium. The supernatants containing lentiviral particles were harvested twice at 48 and 72 hours after transfection, filtered through 0.45-μm filter (Pall Corporation, catalog no. 4184), concentrated using Lenti-X Concentrator (Takara Bio, catalog no. 631231), and stored at −80°C until use.

To infect THP-1 cells with lentiviruses, cells were cultured in medium containing lentiviruses and DEAE-Dextran (20 μg/ml; Sigma-Aldrich, catalog no. 93556). To increase the transduction efficiency, fluorescence-activated cell sorting was performed using a FACSAria II cell sorter from Becton Dickinson equipped with FACSDiva version 8.03. The instrument was set up with a 100-μm nozzle. The sorted populations were gated to exclude double, dead, and autofluorescent cells. The cells were recovered for at least 7 days before performing subsequent experiments.

Cell culture

Human monocytic THP-1 cells were maintained in RPMI 1640 Medium (Thermo Fisher Scientific, catalog no. 11875085), supplemented with heat inactivated 10% fetal bovine serum (FBS) and 0.05 mM 2-mercaptoethanol (Thermo Fisher Scientific, catalog no. 31350010), 10 mM Hepes (Thermo Fisher Scientific, catalog no. 15630080), 1 mM sodium pyruvate (Thermo Fisher Scientific, catalog no. 11360070), penicillin (100 U/ml), and streptomycin (100 μg/ml).

The NLRP3 KO THP-1 cells were purchased from company (InvivoGen, catalog no. thp-konlrp3z). NLRP3 KO THP-1 cells reconstituted with mScarlet-NLRP3 cells were generated via lentivirus infection and flow cytometry sorting as described above, which is used for cryo-ET throughout the manuscript.

All cells were maintained at 37°C with 5% CO_2. For inflammasome activation studies, THP-1 cells were differentiated for 48 hours with 100 nM phorbol myristate acetate (Sigma-Aldrich, catalog no. P8139–5MG), followed by priming for 4 hours with LPSs (1 μg/ml; InvivoGen, catalog no. tlrl-b5lps) before stimulation with 20 μM nigericin (Sigma-Aldrich, catalog no. N7143-10MG) for the indicated times. When needed, 10 μM microtubule polymerization inhibitor Colchicine (Sigma-Aldrich, catalog no. C9754–100MG) or 20 μM HDAC6 inhibitor Tubacin (Sigma-Aldrich, catalog no. SML0065-1MG) was used for 2 hours before nigericin treatment.

Sample preparation for cryo-ET

mScarlet-THP-1 cells were maintained as described in previous section. Cells were differentiated for 24 hours in tissue culture–treated plate and seeded onto human fibronectin [25 μg/ml in 1× phosphate-buffered saline (PBS); Advanced Biomatrix, catalog no. 5050]–coated grids (R2/2, Au 200-mesh London Finder grid coated with extra thick carbon, Electron Microscopy Sciences) for another 24 hours to allow sufficient adherence. On the day of plunge freezing, cells on grids were primed with LPS (1 μg/ml) and stained by SiR-tubulin (1 μM; Cytoskeleton Inc., catalog no. CY-SC002) for 4 hours (*44*). Cells in the treatment group were further treated with 20 μM nigericin for NLRP3 inflammasome activation for 10 to 20 min or 30 to 45 min. Untreated cells were stained by SiR-tubulin only for 4 hours. Grids were plunge frozen in liquid ethane (Airgas) at different time points on a MarkIV vitrobot (Thermo Fisher Scientific) at 100% humidity with manual blotting. Each condition was frozen on the basis of the following order: after 4 hours for both untreated and LPS-treated cells; 4 hours plus 10 to 20 min for LPS + nigericin (Nig) 10 to 20 min–treated cells; and 4 hours plus 30 to 45 min for LPS + Nig > 30 min–treated cells.

In situ fluorescence–guided cryo–FIB-SEM milling

Frozen grids were clipped into AutoGrids with 4 milling slots (Thermo Fisher Scientific) and loaded onto the Airyscan laser scanning microscope (Zeiss LSM880) equipped with a cryo-sample stage (Linkam, CMS196) for inspection of colocalized NLRP3 and MTOC puncta and ice quality. NLRP3 signal was detected by excitation at 555 nm. MTOC signal was detected by excitation at 625 nm. Grids were then transferred to an Aquilos2 Dual-Beam system (Thermo Fisher Scientific) with customized integrated fluorescence light microscope (ENZEL from Delmic B.V.) that is coincident with the

FIB and SEM of the Aquilos2 as described previously (*41*). Organoplatinum (Pt) deposition was applied to grids via the gas injection system for 20 to 30 s. The NLRP3 inflammasome was identified as the colocalized NLRP3 and MTOC puncta observed on the ENZEL system equipped with a 100× long working distance vacuum objective [0.85 numerical aperture (NA)]. Materials above and below the targets of interest were ablated accordingly monitored by real-time fluorescence. The stepwise milling was performed as described in previous studies (*60*, *63*, *64*, *143*). In brief, rough milling, thinning, and polishing were done at 0.1 nA, 30 pA, and10 pA at 30 kV. Final fluorescence images were taken when the thickness of the lamella was ~200 nm with the following imaging parameters: NLRP3, ~0.96 W/cm^2 of 550 ± 10 nm with 1.5- to 2-s exposure; MTOC, ~ 0.46 W/cm^2 of 625 ± 10 nm with 1- to 2-s exposure; and reflected bright field, ~0.1 W/cm^2 of 550 ± 10 nm with 500-ms exposure.

Tilt series acquisition guided by correlated fluorescence microscopy

Atlases and tilt series were acquired on a Titan Krios G2 (Thermo Fisher Scientific) at 300 keV equipped with a K3 Summit detector and BioQuantum postcolumn energy filter (Gatan) operated in counting and dose fractionation mode with 20 eV slit in. Atlases were collected as joint serial sections at ×6500 magnification under low-dose mode in SerialEM software suite (*144*, *145*). Tilt series were collected at a pixel size of 3.465 Å with a total dose of ~120 to 160 electron (e^-)/Å^2, ranging from −48° to 60° to account for a ~6° milling angle with 2° increment using SerialEM. This study included a total of 52 tilt series: 11, 17, 20, and 4 for untreated, LPS, LPS + Nig 10 to 20 min, and LPS + Nig > 30 min, respectively.

Cryo-tomogram reconstruction and quantification of cellular features

Unbinned image frames were preprocessed in WARP with patch motion correction, CTF estimation, and defocus estimation, which ultimately assembled to aligned tilt series with a binning factor of 2 (*146*, *147*). Aligned tilt series were reconstructed manually in IMOD at a pixel size of 13.86 Å with 30 iterations of SIRT-like filter following CTF correction (*148*, *149*). Cryo-tomogram reconstructions containing TGN were loaded in Fiji for measuring cisternae width. Cryo-tomogram reconstructions containing NLRP3-associated vesicles were loaded in IMOD (*148*, *149*). The center of each vesicle was manually set and used the size function to measure the radius of each vesicle in pixel, which later was converted to vesicle diameter in nanometers.

Cryo-tomogram segmentation and visualization

Cryo-tomograms used for segmentation were imported to Dragonfly 2022.2 and subject to Gaussian filtering to enhance image contrast. Training datasets were prepared by manually segmenting several slices containing microtubules, large membrane structure, Golgi stacks, small vesicles, ribosome, and mitochondria. The neural network model was generated with a dimension of 2.5D and three slices. NLRP3 condensate and PCM were segmented using the thresholding tool. Segmented features were exported independently and later processed in Fiji with Gaussian blurring (sigma = 0.8) and imported to ChimeraX (version 1.7.1) for visualization (*150*). Cryo-tomograms containing NLRP3 vesicles were manually segmented in IMOD for microtubules, NLRP3-associated vesicles, and intermediate filaments.

Cryo-correlated fluorescence microscopy

Registration of fluorescence and electron tomography data was performed using a customized toolkit compatible with MATLAB version R2023b. Briefly, multichannel fluorescence images obtained from the ENZEL system were firstly correlated to atlases collected at ×6500 magnification using obvious features (e.g., lamellae edges, visible ice contamination, or grid holes) present in both bright-field optical microscopy and the electron microscopy. A total of 8 to 10 pairs of reference points were selected accordingly for precise correlation. These point pairs were used to calculate a projective transformation to carry the fluorescence data to this low-magnification EM space. Second, a new set of points visible in the registered atlases and in a *z*-projection of the tomographic reconstruction were selected. These points largely included visible cellular features (e.g., large membrane structure, vesicles, mitochondria, or MTOC). A total of 10 to 13 pairs of reference points were manually selected for registration and the computation of a similarity transformation to carry the atlas space into the tomography space. Last, the projective and similarity transformation was serially applied to the fluorescence images to bring the fluorescence images to the tomography space. For visualization, final correlated images containing SiR-tubulin and NLRP3 channels were generated by overlaying fluorescence channels with actual cryo-tomogram reconstruction ($z = 10$).

Vesicle correlation analysis

Correlated atlases and cryo-tomogram reconstructions were computed as described in previous section. Vesicle x and y coordinates were extracted from IMOD segmented models and later correlated with registered cryo-tomogram reconstructions. The number of vesicles within each registered fluorescence pixel was plotted and fitted to a simple linear regression.

LDH cytotoxicity assay

WT THP-1, NLRP3 KO THP-1, and NLRP3 KO THP-1 reconstituted with mScarlet-NLRP3 were seeded on a 24-well plate. After differentiation, priming, and NLRP3 activation, cell supernatants were analyzed for LDH activity using the LDH-Glo Cytotoxicity Assay Kit (Promega, catalog no. J2381) according to the manufacturer's guidelines.

Immunofluorescence and live-cell imaging

To detect protein localization by immunofluorescence in fixed cells, cells were seeded on high-performance no. 1.5 18 mm–by–18 mm glass coverslips (Zeiss, catalog no. 474030-9000-000) and fixed with 4% paraformaldehyde (PFA) for 15 min, followed by permeabilization with 0.5% Triton X-100 for 5 min. Then, cells were blocked with 1.5% bovine serum albumin (BSA) for 1 hour at room temperature. Primary antibodies (ASC, 1:200; AdipoGen, AG25B0006C100; and LC3B, 1:20; Santa Cruz Biotechnology, sc-271625) were diluted in 1.5% BSA and incubated overnight with fixed cells at 4°C. After washing with 1× Dulbecco's Phosphate-Buffered Saline (DPBS) three times, fluorescent secondary antibodies were 1: 1,000 diluted in 1.5% BSA and incubated for 1 hour at room temperature. Samples were mounted in VECTASHIELD antifade mounting medium (Vector Laboratories, catalog no. H-1000-10) and sealed with nail polish (Fisher Scientific, catalog no. NC1849418).

For visualization of NLRP3 inflammasome activation of mSL control and mSL-NLRP3 cells, cells were differentiated and grown

in 35 mm glass bottom dishes (ibidi, catalog no. 81218-200) for 48 hours. Then, cells were first washed once with PBS, and the medium was replaced by RPMI 1640 medium (Gibco, catalog no. 11875093) supplemented with 10% FBS and placed back in the incubator kept at 37°C for at least 1 hour. Cells were stained with 1 μM SiR-Tubulin shortly before LPS priming. Inflammasome activator concentrations were applied as following: 20 mM nigericin, 5 mM ATP (InvivoGen, catalog no. tlrl-atpl), and imiquimod (20 μg/ml; InvivoGen, catalog no. tlrl-imqs-1). Inhibitors were added 2.5 hours after LPS priming and 30 min before activation with 20 μM zVAD-FMK (InvivoGen, catalog no. tlrl-vad) or 5 μM MCC950 (Sigma-Aldrich, catalog no. 5381200001). Activator and inhibitor concentrations and times were adapted from a previous study (*52*). All images were collected with oil-immersion 63× (1.4 NA) lenses mounted on a Zeiss Elyra 7 Lattice Structured Illumination Microscope (SIM).

For visualization of mScarlet-NLRP3, TGN38-mNeonGreen, and SiR-tubulin in live cells, cells were differentiated and grown in 35-mm glass bottom dishes (MatTek corporation, catalog no. P35G-1.5–14-C) for 48 hours. Then, cells were first washed once with PBS, and the medium was replaced by RPMI 1640 medium with no phenol red (Thermo Fisher Scientific, catalog no. 11835030) supplemented with 10% FBS and placed back in the incubator for at least 1 hour. Live-cell images were obtained at 37°C with 5% CO_2 condition. All images were collected with oil-immersion 60× (1.4 NA) lenses on a spinning disk confocal on an inverted Nikon Ti fluorescence microscope, which was equipped with Nikon Perfect Focus System and Yokogawa CSU-X1 Confocal Scanner, and operated with NIS-Elements image acquisition software.

FRAP microscopy

mScarlet-NLRP3 cells together with mNeonGreen-ASC reconstituted NLRP3 KO THP-1 cells were cultured on 35-mm glass-bottomed dishes (MatTek). FRAP microscopy for cytosolic or dTGN-localized NLRP3 before activation and dispersed NLRP3 after 10 min of nigericin treatment was performed on a Deltavision OMX Blaze 3D SIM, equipped with sCMOS Cameras, and six laser beams (405, 445, 488, 514, 568, and 642 nm; 100 mW). To obtain optimal images, immersion oil with refractive indices of 1.516 was used. FRAP microscopy for NLRP3 and ASC specks after 30 min of nigericin treatment was performed on a Leica STELLARIS 8 FALCON FLIM Microscope equipped with a 60× 1.4 NA HC PL APO CS2 oil-immersion objective and operated with the LASX acquisition software. The region of interest was photobleached, and the recovery of fluorescence intensity within the region of interest was obtained for each experiment. Photobleaching and subsequent image acquisition were performed with three prebleached images and a sequence of 120 postbleach images at 1-s intervals. Intensity recovery curves were normalized against photofading outside the bleaching area, calculated as percentage of recovery (*151*, *152*), and fitted with a one phase exponential association curve by GraphPad Prism.

Quantification and statistical analysis

The data used in this study were presented as means ± SD in triplicate experiments unless otherwise stated. Statistical analyses (two-tailed Student's *t* test, Mann-Whitney test, linear regression, and so on) were performed using existing software (GraphPad Prism 9 or 10). $P < 0.05$ was considered significant. Representative microscopy images were obtained from at least six independent cells. For the statistical significance and sample size of all graphs, please see the figure legends.

Supplementary Materials

The PDF file includes:
Figs. S1 to S7
Legends for movies S1 to S7

Other Supplementary Material for this manuscript includes the following:
Movies S1 to S7

REFERENCES

1. J. Fu, H. Wu, Structural mechanisms of NLRP3 inflammasome assembly and activation. *Annu. Rev. Immunol.* **41**, 301–316 (2023).
2. K. V. Swanson, M. Deng, J. P. Ting, The NLRP3 inflammasome: Molecular activation and regulation to therapeutics. *Nat. Rev. Immunol.* **19**, 477–489 (2019).
3. K. Schroder, J. Tschopp, The inflammasomes. *Cell* **140**, 821–832 (2010).
4. M. M. Gaidt, V. Hornung, The NLRP3 inflammasome renders cell death pro-inflammatory. *J. Mol. Biol.* **430**, 133–141 (2018).
5. P. Broz, V. M. Dixit, Inflammasomes: Mechanism of assembly, regulation and signalling. *Nat. Rev. Immunol.* **16**, 407–420 (2016).
6. X. Que, S. Zheng, Q. Song, H. Pei, P. Zhang, Fantastic voyage: The journey of NLRP3 inflammasome activation. *Genes Dis* **11**, 819–829 (2024).
7. Z. Wang, S. Zhang, Y. Xiao, W. Zhang, S. Wu, T. Qin, Y. Yue, W. Qian, L. Li, NLRP3 inflammasome and inflammatory diseases. *Oxid. Med. Cell. Longev.* **2020**, 4063562 (2020).
8. A. Zahid, B. Li, A. J. K. Kombe, T. Jin, J. Tao, Pharmacological inhibitors of the NLRP3 inflammasome. *Front. Immunol.* **10**, 2538 (2019).
9. D. Wu, Z. Zhang, X. Jiang, Y. Du, S. Zhang, X.-D. Yang, Inflammasome meets centrosome: Understanding the emerging role of centrosome in controlling inflammasome activation. *Front. Immunol.* **13**, 826106 (2022).
10. L. Xiao, V. G. Magupalli, H. Wu, Cryo-EM structures of the active NLRP3 inflammasome disc. *Nature* **613**, 595–600 (2023).
11. Y. Dong, J. P. Bonin, P. Devant, Z. Liang, A. I. M. Sever, J. Mintseris, J. M. Aramini, G. Du, S. P. Gygi, J. C. Kagan, L. E. Kay, H. Wu, Structural transitions enable interleukin-18 maturation and signaling. *Immunity* **57**, 1533–1548.e10 (2024).
12. J. Lieberman, H. Wu, J. C. Kagan, Gasdermin D activity in inflammation and host defense. *Sci. Immunol.* **4**, eaav1447 (2019).
13. V. Hornung, A. Ablasser, M. Charrel-Dennis, F. Bauernfeind, G. Horvath, D. R. Caffrey, E. Latz, K. A. Fitzgerald, AIM2 recognizes cytosolic dsDNA and forms a caspase-1-activating inflammasome with ASC. *Nature* **458**, 514–518 (2009).
14. V. G. Magupalli, R. Negro, Y. Tian, A. V. Hauenstein, G. Di Caprio, W. Skillern, Q. Deng, P. Orning, H. B. Alam, Z. Maliga, H. Sharif, J. J. Hu, C. L. Evavold, J. C. Kagan, F. I. Schmidt, K. A. Fitzgerald, T. Kirchhausen, Y. Li, H. Wu, HDAC6 mediates an aggresome-like mechanism for NLRP3 and pyrin inflammasome activation. *Science* **369**, eaas8995 (2020).
15. J. Wu, T. Fernandes-Alnemri, E. S. Alnemri, Involvement of the AIM2, NLRC4, and NLRP3 inflammasomes in caspase-1 activation by *Listeria monocytogenes*. *J. Clin. Immunol.* **30**, 693–702 (2010).
16. X. Li, S. Thome, X. Ma, M. Amrute-Nayak, A. Finigan, L. Kitt, L. Masters, J. R. James, Y. Shi, G. Meng, Z. Mallat, MARK4 regulates NLRP3 positioning and inflammasome activation through a microtubule-dependent mechanism. *Nat. Commun.* **8**, 15986 (2017).
17. Y. He, M. Y. Zeng, D. Yang, B. Motro, G. Núñez, NEK7 is an essential mediator of NLRP3 activation downstream of potassium efflux. *Nature* **530**, 354–357 (2016).
18. H. Shi, Y. Wang, X. Li, X. Zhan, M. Tang, M. Fina, L. Su, D. Pratt, C. H. Bu, S. Hildebrand, S. Lyon, L. Scott, J. Quan, Q. Sun, J. Russell, S. Arnett, P. Jurek, D. Chen, V. V. Kravchenko, J. C. Mathison, E. M. Y. Moresco, N. L. Monson, R. J. Ulevitch, B. Beutler, NLRP3 activation and mitosis are mutually exclusive events coordinated by NEK7, a new inflammasome component. *Nat. Immunol.* **17**, 250–258 (2016).
19. J. L. Schmid-Burgk, D. Chauhan, T. Schmidt, T. S. Ebert, J. Reinhardt, E. Endl, V. Hornung, A genome-wide CRISPR (clustered regularly interspaced short palindromic repeats) screen identifies NEK7 as an essential component of NLRP3 inflammasome activation. *J. Biol. Chem.* **291**, 103–109 (2016).
20. S. Bai, F. Martin-Sanchez, D. Brough, G. Lopez-Castejon, Pyroptosis leads to loss of centrosomal integrity in macrophages. *Cell Death Discov.* **10**, 354 (2024).
21. H. Xian, K. Watari, E. Sanchez-Lopez, J. Offenberger, J. Onyuru, H. Sampath, W. Ying, H. M. Hoffman, G. S. Shadel, M. Karin, Oxidized DNA fragments exit mitochondria via mPTP- and VDAC-dependent channels to activate NLRP3 inflammasome and interferon signaling. *Immunity* **55**, 1370–1385.e8 (2022).
22. S. R. Mishra, K. K. Mahapatra, B. P. Behera, S. Patra, C. S. Bhol, D. P. Panigrahi, P. P. Praharaj, A. Singh, S. Patil, R. Dhiman, S. K. Bhutia, Mitochondrial dysfunction as a driver of NLRP3

inflammasome activation and its modulation through mitophagy for potential therapeutics. *Int. J. Biochem. Cell Biol.* **136**, 106013 (2021).
23. R. Zhou, A. S. Yazdi, P. Menu, J. Tschopp, A role for mitochondria in NLRP3 inflammasome activation. *Nature* **469**, 221–225 (2011).
24. Z. Zhang, R. Venditti, L. Ran, Z. Liu, K. Vivot, A. Schurmann, J. S. Bonifacino, M. A. De Matteis, R. Ricci, Distinct changes in endosomal composition promote NLRP3 inflammasome activation. *Nat. Immunol.* **24**, 30–41 (2023).
25. B. Lee, C. Hoyle, R. Wellens, J. P. Green, F. Martin-Sanchez, D. M. Williams, B. J. Matchett, P. I. Seoane, H. Bennett, A. Adamson, G. Lopez-Castejon, M. Lowe, D. Brough, Disruptions in endocytic traffic contribute to the activation of the NLRP3 inflammasome. *Sci. Signal.* **16**, eabm7134 (2023).
26. H. Sharif, L. Wang, W. L. Wang, V. G. Magupalli, L. Andreeva, Q. Qiao, A. V. Hauenstein, Z. Wu, G. Núñez, Y. Mao, H. Wu, Structural mechanism for NEK7-licensed activation of NLRP3 inflammasome. *Nature* **570**, 338–343 (2019).
27. X. Yu, R. E. Matico, R. Miller, D. Chauhan, B. Van Schoubroeck, K. Grauwen, J. Suarez, B. Pietrak, N. Haloi, Y. Yin, G. J. Tresadern, L. Perez-Benito, E. Lindahl, A. Bottelbergs, D. Oehlrich, N. Van Opdenbosch, S. Sharma, Structural basis for the oligomerization-facilitated NLRP3 activation. *Nat. Commun.* **15**, 1164 (2024).
28. L. Andreeva, L. David, S. Rawson, C. Shen, T. Pasricha, P. Pelegrin, H. Wu, NLRP3 cages revealed by full-length mouse NLRP3 structure control pathway activation. *Cell* **184**, 6299–6312.e22 (2021).
29. I. V. Hochheiser, M. Pilsl, G. Hagelueken, J. Moecking, M. Marleaux, R. Brinkschulte, E. Latz, C. Engel, M. Geyer, Structure of the NLRP3 decamer bound to the cytokine release inhibitor CRID3. *Nature* **604**, 184–189 (2022).
30. U. Ohto, Y. Kamitsukasa, H. Ishida, Z. Zhang, K. Murakami, C. Hirama, S. Maekawa, T. Shimizu, Structural basis for the oligomerization-mediated regulation of NLRP3 inflammasome activation. *Proc. Natl. Acad. Sci. U.S.A.* **119**, e2121353119 (2022).
31. Y. Liu, H. Zhai, H. Alemayehu, J. Boulanger, L. J. Hopkins, A. C. Borgeaud, C. Heroven, J. D. Howe, K. E. Leigh, C. E. Bryant, Y. Modis, Cryo-electron tomography of NLRP3-activated ASC complexes reveals organelle co-localization. *Nat. Commun.* **14**, 7246 (2023).
32. L. Sborgi, F. Ravotti, V. P. Dandey, M. S. Dick, A. Mazur, S. Reckel, M. Chami, S. Scherer, M. Huber, A. Böckmann, E. H. Egelman, H. Stahlberg, P. Broz, B. H. Meier, S. Hiller, Structure and assembly of the mouse ASC inflammasome by combined NMR spectroscopy and cryo-electron microscopy. *Proc. Natl. Acad. Sci. U.S.A.* **112**, 13237–13242 (2015).
33. Y. Li, T. M. Fu, A. Lu, K. Witt, J. Ruan, C. Shen, H. Wu, Cryo-EM structures of ASC and NLRC4 CARD filaments reveal a unified mechanism of nucleation and activation of caspase-1. *Proc. Natl. Acad. Sci. U.S.A.* **115**, 10845–10852 (2018).
34. A. Stutz, G. L. Horvath, B. G. Monks, E. Latz, ASC speck formation as a readout for inflammasome activation. *Methods Mol. Biol.* **1040**, 91–101 (2013).
35. C. M. Hampton, J. D. Strauss, Z. Ke, R. S. Dillard, J. E. Hammonds, E. Alonas, T. M. Desai, M. Marin, R. E. Storms, F. Leon, G. B. Melikyan, P. J. Santangelo, P. W. Spearman, E. R. Wright, Correlated fluorescence microscopy and cryo-electron tomography of virus-infected or transfected mammalian cells. *Nat. Protoc.* **12**, 150–167 (2017).
36. G. H. Wu, P. G. Mitchell, J. G. Galaz-Montoya, C. W. Hecksel, E. M. Sontag, V. Gangadharan, J. Marshman, D. Mankus, M. E. Bisher, A. K. R. Lytton-Jean, J. Frydman, K. Czymmek, W. Chiu, Multi-scale 3D cryo-correlative microscopy for vitrified cells. *Structure* **28**, 1231–1237.e3 (2020).
37. S. D. Carter, J. I. Mamede, T. J. Hope, G. J. Jensen, Correlated cryogenic fluorescence microscopy and electron cryo-tomography shows that exogenous TRIM5α can form hexagonal lattices or autophagy aggregates in vivo. *Proc. Natl. Acad. Sci. U.S.A.* **117**, 29702–29711 (2020).
38. J. Arnold, J. Mahamid, V. Lucic, A. de Marco, J. J. Fernandez, T. Laugks, T. Mayer, A. A. Hyman, W. Baumeister, J. M. Plitzko, Site-specific cryo-focused ion beam sample preparation guided by 3D correlative microscopy. *Biophys. J.* **110**, 860–869 (2016).
39. J. E. Yang, M. R. Larson, B. S. Sibert, S. Shrum, E. R. Wright, CorRelator: Interactive software for real-time high precision cryo-correlative light and electron microscopy. *J. Struct. Biol.* **213**, 107709 (2021).
40. X. Fu, J. Ning, Z. Zhong, Z. Ambrose, S. Charles Watkins, P. Zhang, AutoCLEM: An automated workflow for correlative live-cell fluorescence microscopy and cryo-electron tomography. *Sci. Rep.* **9**, 19207 (2019).
41. D. B. Boltje, J. P. Hoogenboom, A. J. Jakobi, G. J. Jensen, C. T. H. Jonker, M. J. Kaag, A. J. Koster, M. G. F. Last, C. de Agrela Pinto, J. M. Plitzko, S. Raunser, S. Tacke, Z. Wang, E. B. van der Wee, R. Wepf, S. den Hoedt, A cryogenic, coincident fluorescence, electron, and ion beam microscope. *eLife* **11**, e82891 (2022).
42. M. Lamkanfi, V. M. Dixit, Mechanisms and functions of inflammasomes. *Cell* **157**, 1013–1022 (2014).
43. R. Muñoz-Planillo, P. Kuffa, G. Martínez-Colón, B. L. Smith, T. M. Rajendiran, G. Núñez, K^+ efflux is the common trigger of NLRP3 inflammasome activation by bacterial toxins and particulate matter. *Immunity* **38**, 1142–1153 (2013).
44. G. Lukinavičius, L. Reymond, E. D'Este, A. Masharina, F. Göttfert, H. Ta, A. Güther, M. Fournier, S. Rizzo, H. Waldmann, C. Blaukopf, C. Sommer, D. W. Gerlich, H.-D. Arndt, S. W. Hell, K. Johnsson, Fluorogenic probes for live-cell imaging of the cytoskeleton. *Nat. Methods* **11**, 731–733 (2014).
45. M. Mateo-Tórtola, I. V. Hochheiser, J. Grga, J. S. Mueller, M. Geyer, A. N. R. Weber, A. Tapia-Abellán, Non-decameric NLRP3 forms an MTOC-independent inflammasome. bioRxiv 548075 [Preprint] (2023). https://doi.org/10.1101/2023.07.07.548075.
46. R. Brinkschulte, D. M. Fußhöller, F. Hoss, J. F. Rodríguez-Alcázar, M. A. Lauterbach, C. C. Kolbe, M. Rauen, S. Ince, C. Herrmann, E. Latz, M. Geyer, ATP-binding and hydrolysis of human NLRP3. *Commun. Biol.* **5**, 1176 (2022).
47. T. Zhang, H. Tsutsuki, W. Islam, K. Ono, K. Takeda, T. Akaike, T. Sawa, ATP exposure stimulates glutathione efflux as a necessary switch for NLRP3 inflammasome activation. *Redox Biol.* **41**, 101930 (2021).
48. Q.-B. Zha, H.-X. Wei, C.-G. Li, Y.-D. Liang, L.-H. Xu, W.-J. Bai, H. Pan, X.-H. He, D.-Y. Ouyang, ATP-induced inflammasome activation and pyroptosis is regulated by AMP-activated protein kinase in macrophages. *Front. Immunol.* **7**, 597 (2016).
49. A. Di, S. Xiong, Z. Ye, R. K. S. Malireddi, S. Kometani, M. Zhong, M. Mittal, Z. Hong, T. D. Kanneganti, J. Rehman, A. B. Malik, The TWIK2 potassium efflux channel in macrophages mediates NLRP3 inflammasome-induced inflammation. *Immunity* **49**, 56–65.e4 (2018).
50. P. Pelegrin, A. Surprenant, Pannexin-1 couples to maitotoxin- and nigericin-induced interleukin-1beta release through a dye uptake-independent pathway. *J. Biol. Chem.* **282**, 2386–2394 (2007).
51. A. Surprenant, F. Rassendren, E. Kawashima, R. A. North, G. Buell, The cytolytic P2Z receptor for extracellular ATP identified as a P2X receptor (P2X7). *Science* **272**, 735–738 (1996).
52. C. J. Groß, R. Mishra, K. S. Schneider, G. Médard, J. Wettmarshausen, D. C. Dittlein, H. Shi, O. Gorka, P. A. Koenig, S. Fromm, G. Magnani, T. Ćiković, L. Hartjes, J. Smollich, A. A. B. Robertson, M. A. Cooper, M. Schmidt-Supprian, M. Schuster, K. Schroder, P. Broz, C. Traidi-Hoffmann, B. Beutler, B. Kuster, J. Ruland, S. Schneider, F. Perocchi, O. Groß, K^+ efflux-independent NLRP3 inflammasome activation by small Molecules targeting mitochondria. *Immunity* **45**, 761–773 (2016).
53. H. Hemmi, T. Kaisho, O. Takeuchi, S. Sato, H. Sanjo, K. Hoshino, T. Horiuchi, H. Tomizawa, K. Takeda, S. Akira, Small anti-viral compounds activate immune cells via the TLR7 MyD88-dependent signaling pathway. *Nat. Immunol.* **3**, 196–200 (2002).
54. M. Pizzuto, P. Pelegrin, J.-M. Ruysschaert, Lipid-protein interactions regulating the canonical and the non-canonical NLRP3 inflammasome. *Prog. Lipid Res.* **87**, 101182 (2022).
55. R. C. Coll, A. A. Robertson, J. J. Chae, S. C. Higgins, R. Muñoz-Planillo, M. C. Inserra, I. Vetter, L. S. Dungan, B. G. Monks, A. Stutz, D. E. Croker, M. S. Butler, M. Haneklaus, C. E. Sutton, G. Núñez, E. Latz, D. L. Kastner, K. H. Mills, S. L. Masters, K. Schroder, M. A. Cooper, L. A. O'Neill, A small-molecule inhibitor of the NLRP3 inflammasome for the treatment of inflammatory diseases. *Nat. Med.* **21**, 248–255 (2015).
56. R. C. Coll, J. R. Hill, C. J. Day, A. Zamoshnikova, D. Boucher, N. L. Massey, J. L. Chitty, J. A. Fraser, M. P. Jennings, A. A. B. Robertson, K. Schroder, MCC950 directly targets the NLRP3 ATP-hydrolysis motif for inflammasome inhibition. *Nat. Chem. Biol.* **15**, 556–559 (2019).
57. M. M. Gaidt, T. S. Ebert, D. Chauhan, T. Schmidt, J. L. Schmid-Burgk, F. Rapino, A. A. Robertson, M. A. Cooper, T. Graf, V. Hornung, Human monocytes engage an alternative inflammasome pathway. *Immunity* **44**, 833–846 (2016).
58. J.-H. Kim, H.-J. Sohn, J.-K. Yoo, H. Kang, G.-S. Seong, Y.-J. Chwae, K. Kim, S. Park, H.-J. Shin, NLRP3 inflammasome activation in THP-1 target cells triggered by pathogenic *Naegleria fowleri*. *Infect. Immun.* **84**, 2422–2428 (2016).
59. E. A. Slee, H. Zhu, S. C. Chow, M. MacFarlane, D. W. Nicholson, G. M. Cohen, Benzyloxycarbonyl-Val-Ala-Asp (OMe) fluoromethylketone (Z-VAD.FMK) inhibits apoptosis by blocking the processing of CPP32. *Biochem. J.* **315**, 21–24 (1996).
60. J. Wang, A. V. Sica, G. J. Jensen, P. D. Dahlberg, Workflow using a cryogenic coincident fluorescence, electron, and ion beam microscope for targeted milling of cells. *J. Vis. Exp.*, 10.3791/68238 (2025).
61. C. L. McCafferty, S. Klumpe, R. E. Amaro, W. Kukulski, L. Collinson, B. D. Engel, Integrating cellular electron microscopy with multimodal data to explore biology across space and time. *Cell* **187**, 563–584 (2024).
62. C. Lin, L. Zhang, Z. Zhang, Y. Jiang, X. Li, Locating cellular contents during cryoFIB milling using cellular secondary-electron imaging. *J. Struct. Biol.* **215**, 108005 (2023).
63. A. V. Sica, M. Zaoralová, C. Antolini, D. B. Boltje, J. J. Penzes, L. M. Malmqvist, G. Jensen, J. T. Kaelber, P. Dahlberg, Optical interference for the guidance of cryogenic focused ion beam milling beyond the axial diffraction limit. bioRxiv 621231 [Preprint] (2024). https://doi.org/10.1101/2024.11.01.621231.
64. V. Lam, E. Villa, Practical approaches for cryo-FIB milling and applications for cellular cryo-electron tomography. *Methods Mol. Biol.* **2215**, 49–82 (2021).

65. S. Li, Z. Wang, X. Jia, T. Niu, J. Zhang, G. Yin, X. Zhang, Y. Zhu, G. Ji, F. Sun, ELI trifocal microscope: A precise system to prepare target cryo-lamellae for in situ cryo-ET study. *Nat. Methods* **20**, 276–283 (2023).
66. F. Tollervey, M. U. Rios, E. Zagoriy, J. B. Woodruff, J. Mahamid, Molecular architectures of centrosomes in *C. elegans* embryos visualized by cryo-electron tomography. *Dev. Cell* **60**, 885–900.e5 (2025).
67. X. Zhang, S. Sridharan, I. Zagoriy, C. Eugster Oegema, C. Ching, T. Pflaesterer, H. K. H. Fung, I. Becher, I. Poser, C. W. Müller, A. A. Hyman, M. M. Savitski, J. Mahamid, Molecular mechanisms of stress-induced reactivation in mumps virus condensates. *Cell* **186**, 1877–1894.e27 (2023).
68. Q. Guo, C. Lehmer, A. Martínez-Sánchez, T. Rudack, F. Beck, H. Hartmann, M. Pérez-Berlanga, F. Frottin, M. S. Hipp, F. U. Hartl, D. Edbauer, W. Baumeister, R. Fernández-Busnadiego, In situ structure of neuronal C9orf72 poly-GA aggregates reveals proteasome recruitment. *Cell* **172**, 696–705.e12 (2018).
69. M. H. Laporte, D. Gambarotto, É. Bertiaux, L. Bournonville, V. Louvel, J. M. Nunes, S. Borgers, V. Hamel, P. Guichard, Time-series reconstruction of the molecular architecture of human centriole assembly. *Cell* **187**, 2158–2174.e19 (2024).
70. M. LeGuennec, N. Klena, G. Aeschlimann, V. Hamel, P. Guichard, Overview of the centriole architecture. *Curr. Opin. Struct. Biol.* **66**, 58–65 (2021).
71. M. Paintrand, M. Moudjou, H. Delacroix, M. Bornens, Centrosome organization and centriole architecture: Their sensitivity to divalent cations. *J. Struct. Biol.* **108**, 107–128 (1992).
72. H. Fujita, Y. Yoshino, N. Chiba, Regulation of the centrosome cycle. *Mol. Cell. Oncol.* **3**, e1075643 (2016).
73. M. T. Bertran, S. Sdelci, L. Regué, J. Avruch, C. Caelles, J. Roig, Nek9 is a Plk1-activated kinase that controls early centrosome separation through Nek6/7 and Eg5. *EMBO J.* **30**, 2634–2647 (2011).
74. E. Smith, N. Hégarat, C. Vesely, I. Roseboom, C. Larch, H. Streicher, K. Straatman, H. Flynn, M. Skehel, T. Hirota, R. Kuriyama, H. Hochegger, Differential control of Eg5-dependent centrosome separation by Plk1 and Cdk1. *EMBO J.* **30**, 2233–2245 (2011).
75. E. Vitiello, P. Moreau, V. Nunes, A. Mettouchi, H. Maiato, J. G. Ferreira, I. Wang, M. Balland, Acto-myosin force organization modulates centriole separation and PLK4 recruitment to ensure centriole fidelity. *Nat. Commun.* **10**, 52 (2019).
76. C. Prigent, R. Uzbekov, Duplication and segregation of centrosomes during cell division. *Cells* **11**, 2445 (2022).
77. H.-J. Nam, R. M. Naylor, J. M. van Deursen, Centrosome dynamics as a source of chromosomal instability. *Trends Cell Biol.* **25**, 65–73 (2015).
78. D. Hossain, S. Y.-P. Shih, X. Xiao, J. White, W. Y. Tsang, Cep44 functions in centrosome cohesion by stabilizing rootletin. *J. Cell Sci.* **133**, jcs239616 (2020).
79. Y. Wang, P. Ji, J. Liu, R. R. Broaddus, F. Xue, W. Zhang, Centrosome-associated regulators of the G2/M checkpoint as targets for cancer therapy. *Mol. Cancer* **8**, 8 (2009).
80. A. Shukla, D. Kong, M. Sharma, V. Magidson, J. Loncarek, Plk1 relieves centriole block to reduplication by promoting daughter centriole maturation. *Nat. Commun.* **6**, 8077 (2015).
81. X. Jiang, D. B. T. Ho, K. Mahe, J. Mia, G. Sepulveda, M. Antkowiak, L. Jiang, S. Yamada, L. E. Jao, Condensation of pericentrin proteins in human cells illuminates phase separation in centrosome assembly. *J. Cell Sci.* **134**, jcs258897 (2021).
82. J. B. Woodruff, B. Ferreira Gomes, P. O. Widlund, J. Mahamid, A. Honigmann, A. A. Hyman, The centrosome is a selective condensate that nucleates microtubules by concentrating tubulin. *Cell* **169**, 1066–1077.e10 (2017).
83. T. Consolati, J. Locke, J. Roostalu, Z. A. Chen, J. Gannon, J. Asthana, W. M. Lim, F. Martino, M. A. Cvetkovic, J. Rappsilber, A. Costa, T. Surrey, Microtubule nucleation properties of single human γTuRCs explained by their cryo-EM structure. *Dev. Cell* **53**, 603–617.e8 (2020).
84. V. Guillet, M. Knibiehler, L. Gregory-Pauron, M. H. Remy, C. Chemin, B. Raynaud-Messina, C. Bon, J. M. Kollman, D. A. Agard, A. Merdes, L. Mourey, Crystal structure of γ-tubulin complex protein GCP4 provides insight into microtubule nucleation. *Nat. Struct. Mol. Biol.* **18**, 915–919 (2011).
85. J. M. Kollman, A. Merdes, L. Mourey, D. A. Agard, Microtubule nucleation by γ-tubulin complexes. *Nat. Rev. Mol. Cell Biol.* **12**, 709–721 (2011).
86. A. Vertii, M. Ivshina, W. Zimmerman, H. Hehnly, S. Kant, S. Doxsey, The centrosome undergoes Plk1-independent interphase maturation during inflammation and mediates cytokine release. *Dev. Cell* **37**, 377–386 (2016).
87. M. S. Ladinsky, D. N. Mastronarde, J. R. McIntosh, K. E. Howell, L. A. Staehelin, Golgi structure in three dimensions: Functional insights from the normal rat kidney cell. *J. Cell Biol.* **144**, 1135–1149 (1999).
88. M. H. Dunlop, A. M. Ernst, L. K. Schroeder, D. K. Toomre, G. Lavieu, J. E. Rothman, Land-locked mammalian Golgi reveals cargo transport between stable cisternae. *Nat. Commun.* **8**, 432 (2017).
89. D. M. Williams, A. A. Peden, S-acylation of NLRP3 provides a nigericin sensitive gating mechanism that controls access to the Golgi. bioRxiv 566891 [Preprint] (2023). https://doi.org/10.1101/2023.11.14.566891.
90. N. A. Schmacke, F. O'Duill, M. M. Gaidt, I. Szymanska, J. M. Kamper, J. L. Schmid-Burgk, S. C. Mädler, T. Mackens-Kiani, T. Kozaki, D. Chauhan, D. Nagl, C. A. Stafford, H. Harz, A. L. Fröhlich, F. Pinci, F. Ginhoux, R. Beckmann, M. Mann, H. Leonhardt, V. Hornung, IKKβ primes inflammasome formation by recruiting NLRP3 to the trans-Golgi network. *Immunity* **55**, 2271–2284.e7 (2022).
91. D. M. Williams, A. A. Peden, S-acylation of NLRP3 provides a nigericin sensitive gating mechanism that controls access to the Golgi. *eLife* **13**, RP94302 (2024).
92. J. Chen, Z. J. Chen, PtdIns4P on dispersed trans-Golgi network mediates NLRP3 inflammasome activation. *Nature* **564**, 71–76 (2018).
93. G. dos Santos, M. R. Rogel, M. A. Baker, J. R. Troken, D. Urich, L. Morales-Nebreda, J. A. Sennello, M. A. Kutuzov, A. Sitikov, J. M. Davis, A. P. Lam, P. Cheresh, D. Kamp, D. K. Shumaker, G. R. S. Budinger, K. M. Ridge, Vimentin regulates activation of the NLRP3 inflammasome. *Nat. Commun.* **6**, 6574 (2015).
94. T. Lang, J. P. W. Lee, K. Elgass, A. A. Pinar, M. D. Tate, E. H. Aitken, H. Fan, S. J. Creed, N. S. Deen, D. A. K. Traore, I. Mueller, D. Stanisic, F. S. Baiwog, C. Skene, M. C. J. Wilce, A. Mansell, E. F. Morand, J. Harris, Macrophage migration inhibitory factor is required for NLRP3 inflammasome activation. *Nat. Commun.* **9**, 2223 (2018).
95. P. Gurung, J. R. Lukens, T. D. Kanneganti, Mitochondria: Diversity in the regulation of the NLRP3 inflammasome. *Trends Mol. Med.* **21**, 193–201 (2015).
96. Q. Liu, D. Zhang, D. Hu, X. Zhou, Y. Zhou, The role of mitochondria in NLRP3 inflammasome activation. *Mol. Immunol.* **103**, 115–124 (2018).
97. M. Yabal, D. J. Calleja, D. S. Simpson, K. E. Lawlor, Stressing out the mitochondria: Mechanistic insights into NLRP3 inflammasome activation. *J. Leukoc. Biol.* **105**, 377–399 (2019).
98. A. Kaasik, D. Safiulina, A. Zharkovsky, V. Veksler, Regulation of mitochondrial matrix volume. *Am. J. Physiol. Cell Physiol.* **292**, C157–C163 (2007).
99. P. Huang, T. Yu, Y. Yoon, Mitochondrial clustering induced by overexpression of the mitochondrial fusion protein Mfn2 causes mitochondrial dysfunction and cell death. *Eur. J. Cell Biol.* **86**, 289–302 (2007).
100. Y. Huo, W. Sun, T. Shi, S. Gao, M. Zhuang, The MFN1 and MFN2 mitofusins promote clustering between mitochondria and peroxisomes. *Commun. Biol.* **5**, 423 (2022).
101. S. Agarwal, S. Ganesh, Perinuclear mitochondrial clustering, increased ROS levels, and HIF1 are required for the activation of HSF1 by heat stress. *J. Cell Sci.* **133**, jcs245589 (2020).
102. A. B. Al-Mehdi, V. M. Pastukh, B. M. Swiger, D. J. Reed, M. R. Patel, G. C. Bardwell, V. V. Pastukh, M. F. Alexeyev, M. N. Gillespie, Perinuclear mitochondrial clustering creates an oxidant-rich nuclear domain required for hypoxia-induced transcription. *Sci. Signal.* **5**, ra47 (2012).
103. G. Du, L. B. Healy, L. David, C. Walker, T. J. El-Baba, C. A. Lutomski, B. Goh, B. Gu, X. Pi, P. Devant, P. Fontana, Y. Dong, X. Ma, R. Miao, A. Balasubramanian, R. Puthenveetil, A. Banerjee, H. R. Luo, J. C. Kagan, S. F. Oh, C. V. Robinson, J. Lieberman, H. Wu, ROS-dependent S-palmitoylation activates cleaved and intact gasdermin D. *Nature* **630**, 437–446 (2024).
104. R. Miao, C. Jiang, W. Y. Chang, H. Zhang, J. An, F. Ho, P. Chen, C. Junqueira, D. Amgalan, F. G. Liang, J. Zhang, C. L. Evavold, I. Hafner-Bratkovič, Z. Zhang, P. Fontana, S. Xia, M. Waldeck-Weiermair, Y. Pan, T. Michel, L. Bar-Peled, H. Wu, J. C. Kagan, R. N. Kitsis, P. Zhang, X. Liu, J. Lieberman, Gasdermin D permeabilization of mitochondrial inner and outer membranes accelerates and enhances pyroptosis. *Immunity* **56**, 2523–2541.e8 (2023).
105. B. C. Creekmore, K. Kixmoeller, B. E. Black, E. B. Lee, Y.-W. Chang, Ultrastructure of human brain tissue vitrified from autopsy revealed by cryo-ET with cryo-plasma FIB milling. *Nat. Commun.* **15**, 2660 (2024).
106. M. Li, I. Tripathi-Giesgen, B. A. Schulman, W. Baumeister, F. Wilfling, In situ snapshots along a mammalian selective autophagy pathway. *Proc. Natl. Acad. Sci. U.S.A.* **120**, e2221712120 (2023).
107. S. Kageyama, S. R. Gudmundsson, Y.-S. Sou, Y. Ichimura, N. Tamura, S. Kazuno, T. Ueno, Y. Miura, D. Noshiro, M. Abe, T. Mizushima, N. Miura, S. Okuda, H. Motohashi, J. A. Lee, K. Sakimura, T. Ohe, N. N. Noda, S. Waguri, E. L. Eskelinen, M. Komatsu, p62/SQSTM1-droplet serves as a platform for autophagosome formation and anti-oxidative stress response. *Nat. Commun.* **12**, 16 (2021).
108. M. Hayashi-Nishino, N. Fujita, T. Noda, A. Yamaguchi, T. Yoshimori, A. Yamamoto, A subdomain of the endoplasmic reticulum forms a cradle for autophagosome formation. *Nat. Cell Biol.* **11**, 1433–1437 (2009).
109. M. Hayashi-Nishino, N. Fujita, T. Noda, A. Yamaguchi, T. Yoshimori, A. Yamamoto, Electron tomography reveals the endoplasmic reticulum as a membrane source for autophagosome formation. *Autophagy* **6**, 301–303 (2010).
110. A. Danieli, S. Martens, p62-mediated phase separation at the intersection of the ubiquitin-proteasome system and autophagy. *J. Cell Sci.* **131**, jcs214304 (2018).
111. D. Sun, R. Wu, J. Zheng, P. Li, L. Yu, Polyubiquitin chain-induced p62 phase separation drives autophagic cargo segregation. *Cell Res.* **28**, 405–415 (2018).
112. G. Zaffagnini, A. Savova, A. Danieli, J. Romanov, S. Tremel, M. Ebner, T. Peterbauer, M. Sztacho, R. Trapannone, A. K. Tarafder, C. Sachse, S. Martens, p62 filaments capture and present ubiquitinated cargos for autophagy. *EMBO J.* **37**, e98308 (2018).

113. J. Wang, S. Chen, M. Liu, M. Zhang, X. Jia, NEK7: A new target for the treatment of multiple tumors and chronic inflammatory diseases. *Inflammopharmacology* **30**, 1179–1187 (2022).
114. Z. Sun, W. Gong, Y. Zhang, Z. Jia, Physiological and pathological roles of mammalian NEK7. *Front. Physiol.* **11**, 606996 (2020).
115. X.-D. Yang, W. Li, S. Zhang, D. Wu, X. Jiang, R. Tan, X. Niu, Q. Wang, X. Wu, Z. Liu, L.-F. Chen, J. Qin, B. Su, PLK4 deubiquitination by Spata2-CYLD suppresses NEK7-mediated NLRP3 inflammasome activation at the centrosome. *EMBO J.* **39**, e102201 (2020).
116. A. M. Fry, L. O'Regan, S. R. Sabir, R. Bayliss, Cell cycle regulation by the NEK family of protein kinases. *J. Cell Sci.* **125**, 4423–4433 (2012).
117. M. Baldrighi, C. Doreth, Y. Li, X. Zhao, E. Warner, H. Chenoweth, K. Kishore, Y. Umrania, D. P. Minde, S. Thome, X. Yu, Y. Lu, A. Knapton, J. Harrison, M. Clarke, E. Latz, G. de Cárcer, M. Malumbres, B. Ryffel, C. Bryant, J. Liu, K. S. Lilley, Z. Mallat, X. Li, PLK1 inhibition dampens NLRP3 inflammasome-elicited response in inflammatory disease models. *J. Clin. Invest.* **133**, e162129 (2023).
118. S. Bai, F. Martin-Sanchez, D. Brough, G. Lopez-Castejon, Pyroptosis leads to loss of centrosomal integrity in macrophages. bioRxiv 568260 [Preprint] (2023). https://doi.org/10.1101/2023.11.22.568260.
119. L. Cui, H. Li, Y. Xi, Q. Hu, H. Liu, J. Fan, Y. Xiang, X. Zhang, W. Shui, Y. Lai, Vesicle trafficking and vesicle fusion: Mechanisms, biological functions, and their implications for potential disease therapy. *Mol. Biomed.* **3**, 29 (2022).
120. R. Fernández-Busnadiego, B. Zuber, U. E. Maurer, M. Cyrklaff, W. Baumeister, V. Lucic, Quantitative analysis of the native presynaptic cytomatrix by cryoelectron tomography. *J. Cell Biol.* **188**, 145–156 (2010).
121. J. C. Nelson, A. K. Stavoe, D. A. Colón-Ramos, The actin cytoskeleton in presynaptic assembly. *Cell Adh. Migr.* **7**, 379–387 (2013).
122. H. Qiu, X. Wu, X. Ma, S. Li, Q. Cai, M. Ganzella, L. Ge, H. Zhang, M. Zhang, Short-distance vesicle transport via phase separation. *Cell* **187**, 2175–2193.e21 (2024).
123. D. Milovanovic, Y. Wu, X. Bian, P. De Camilli, A liquid phase of synapsin and lipid vesicles. *Science* **361**, 604–607 (2018).
124. T. C. Südhof, P. De Camilli, H. Niemann, R. Jahn, Membrane fusion machinery: Insights from synaptic proteins. *Cell* **75**, 1–4 (1993).
125. F. Navone, P. Greengard, P. De Camilli, Synapsin I in nerve terminals: Selective association with small synaptic vesicles. *Science* **226**, 1209–1211 (1984).
126. S. Alberti, A. A. Hyman, Biomolecular condensates at the nexus of cellular stress, protein aggregation disease and ageing. *Nat. Rev. Mol. Cell Biol.* **22**, 196–213 (2021).
127. D. M. Shapiro, M. Ney, S. A. Eghtesadi, A. Chilkoti, Protein phase separation arising from intrinsic disorder: First-principles to bespoke applications. *J. Phys. Chem. B* **125**, 6740–6759 (2021).
128. F. Garcia Quiroz, N. K. Li, S. Roberts, P. Weber, M. Dzuricky, I. Weitzhandler, Y. G. Yingling, A. Chilkoti, Intrinsically disordered proteins access a range of hysteretic phase separation behaviors. *Sci. Adv.* **5**, eaax5177 (2019).
129. M. Du, Z. J. Chen, DNA-induced liquid phase condensation of cGAS activates innate immune signaling. *Science* **361**, 704–709 (2018).
130. F. Jobe, J. Simpson, P. Hawes, E. Guzman, D. Bailey, Respiratory syncytial virus sequesters NF-κB subunit p65 to cytoplasmic inclusion bodies to inhibit innate immune signaling. *J. Virol.* **94**, e01380-20 (2020).
131. C. Shen, R. Li, R. Negro, J. Cheng, S. M. Vora, T. M. Fu, A. Wang, K. He, L. Andreeva, P. Gao, Z. Tian, R. A. Flavell, S. Zhu, H. Wu, Phase separation drives RNA virus-induced activation of the NLRP6 inflammasome. *Cell* **184**, 5759–5774.e20 (2021).
132. X. Su, J. A. Ditlev, E. Hui, W. Xing, S. Banjade, J. Okrut, D. S. King, J. Taunton, M. K. Rosen, R. D. Vale, Phase separation of signaling molecules promotes T cell receptor signal transduction. *Science* **352**, 595–599 (2016).
133. X. Yu, L. Zhang, J. Shen, Y. Zhai, Q. Jiang, M. Yi, X. Deng, Z. Ruan, R. Fang, Z. Chen, X. Ning, Z. Jiang, The STING phase-separator suppresses innate immune signalling. *Nat. Cell Biol.* **23**, 330–340 (2021).
134. G. Zou, Y. Tang, J. Yang, S. Fu, Y. Li, X. Ren, N. Zhou, W. Zhao, J. Gao, Z. Ruan, Z. Jiang, Signal-induced NLRP3 phase separation initiates inflammasome activation. *Cell Res.* **35**, 437–452 (2025).
135. T. Yu, D. Hou, J. Zhao, X. Lu, W. K. Greentree, Q. Zhao, M. Yang, D.-G. Conde, M. E. Linder, H. Lin, NLRP3 Cys126 palmitoylation by ZDHHC7 promotes inflammasome activation. *Cell Rep.* **43**, 114070 (2024).
136. A. C. Borgeaud, I. Ganeva, C. Klein, A. Stooss, D. Ross-Kaschitza, L. Wu, J. S. Riley, S. W. G. Tait, T. Lemmin, T. Kaufmann, W. Kukulski, Large transient assemblies of Apaf1 constitute the apoptosome in cells. bioRxiv 600688 [Preprint] (2024). https://doi.org/10.1101/2024.07.01.600688.
137. T. C. Cheng, C. Hong, I. V. Akey, S. Yuan, C. W. Akey, A near atomic structure of the active human apoptosome. *eLife* **5**, e17755 (2016).
138. T. C. Cheng, I. V. Akey, S. Yuan, Z. Yu, S. J. Ludtke, C. W. Akey, A near-atomic structure of the dark apoptosome provides insight into assembly and activation. *Structure* **25**, 40–52 (2017).
139. L. Dorstyn, C. W. Akey, S. Kumar, New insights into apoptosome structure and function. *Cell Death Differ.* **25**, 1194–1208 (2018).
140. Y. Li, M. Zhou, Q. Hu, X. C. Bai, W. Huang, S. H. Scheres, Y. Shi, Mechanistic insights into caspase-9 activation by the structure of the apoptosome holoenzyme. *Proc. Natl. Acad. Sci. U.S.A.* **114**, 1542–1547 (2017).
141. S. Yuan, X. Yu, M. Topf, S. J. Ludtke, X. Wang, C. W. Akey, Structure of an apoptosome-procaspase-9 CARD complex. *Structure* **18**, 571–583 (2010).
142. L. Zhang, S. Chen, J. Ruan, J. Wu, A. B. Tong, Q. Yin, Y. Li, L. David, A. Lu, W. L. Wang, C. Marks, Q. Ouyang, X. Zhang, Y. Mao, H. Wu, Cryo-EM structure of the activated NAIP2-NLRC4 inflammasome reveals nucleated polymerization. *Science* **350**, 404–409 (2015).
143. F. R. Wagner, R. Watanabe, R. Schampers, D. Singh, H. Persoon, M. Schaffer, P. Fruhstorfer, J. Plitzko, E. Villa, Preparing samples from whole cells using focused-ion-beam milling for cryo-electron tomography. *Nat. Protoc.* **15**, 2041–2070 (2020).
144. D. N. Mastronarde, SerialEM: A program for automated tilt series acquisition on tecnai microscopes using prediction of specimen position. *Microsc. Microanal.* **9**, 1182–1183 (2003).
145. D. N. Mastronarde, Automated electron microscope tomography using robust prediction of specimen movements. *J. Struct. Biol.* **152**, 36–51 (2005).
146. D. Tegunov, P. Cramer, Real-time cryo-electron microscopy data preprocessing with Warp. *Nat. Methods* **16**, 1146–1152 (2019).
147. D. Tegunov, L. Xue, C. Dienemann, P. Cramer, J. Mahamid, Multi-particle cryo-EM refinement with M visualizes ribosome-antibiotic complex at 3.5 Å in cells. *Nat. Methods* **18**, 186–193 (2021).
148. J. R. Kremer, D. N. Mastronarde, J. R. McIntosh, Computer visualization of three-dimensional image data using IMOD. *J. Struct. Biol.* **116**, 71–76 (1996).
149. D. N. Mastronarde, S. R. Held, Automated tilt series alignment and tomographic reconstruction in IMOD. *J. Struct. Biol.* **197**, 102–113 (2017).
150. E. C. Meng, T. D. Goddard, E. F. Pettersen, G. S. Couch, Z. J. Pearson, J. H. Morris, T. E. Ferrin, UCSF ChimeraX: Tools for structure building and analysis. *Protein Sci.* **32**, e4792 (2023).
151. M. Dundr, U. Hoffmann-Rohrer, Q. Hu, I. Grummt, L. I. Rothblum, R. D. Phair, T. Misteli, A kinetic framework for a mammalian RNA polymerase in vivo. *Science* **298**, 1623–1626 (2002).
152. R. D. Phair, S. A. Gorski, T. Misteli, Measurement of dynamic protein binding to chromatin in vivo, using photobleaching microscopy. *Methods Enzymol.* **375**, 393–414 (2004).

Acknowledgments: We express our gratitude to Delmic B.V. for developing and supporting the tri-coincident cryo–FIB-SEM platform. We acknowledge the Stanford-SLAC Cryo-EM Center and Stanford University Cryo-Electron Microscopy Center (cEMc) for instrumentation with special thanks to C. Zhang and L.-M. Joubert. We thank the Core for Imaging Technology & Education (CITE) and Microscopy Resources On the North Quad (MicRoN) at Harvard Medical School for help with light microscopy and the Caltech Cryo-EM Facility for instrumentation in the initial phases of this project. Scientific illustrations were created with BioRender (www.biorender.com). **Funding:** This work was supported, in part, by the National Institutes of Health (AI127401 to G.J.J., AI177778 to H.W., AR079766 to V.G.M., R01GM150905 to M.C., and the Cancer Research Institute Postdoctoral Fellowship to M.W.), grant 2021-234593 from the Chan Zukerberg Initiative DAF advised fund of Silicon Valley Community Foundation (to P.D.D.), the Panofsky Fellowship at the SLAC National Accelerator Laboratory as part of the Department of Energy Laboratory Directed Research and Development program under contract DE-AC02-76SF00515 (to P.D.D.), and Boston Children's Hospital Office of Faculty Development/Basic & Clinical Translational Research Executive Committees Faculty Career Development Fellowship (to V.G.M.). V.G.M. acknowledges support from the Lindsley F. Kimball Research Institute/New York Blood Center Enterprises (NYBCe) startup funds. **Author contributions:** Conceptualization: J.W., V.G.M., H.W., and G.J.J. Methodology: J.W., M.W., L.X., G.D., M.C., V.G.M., P.D.D., H.W., and G.J.J. Data curation: J.W., M.W., L.X., G.D., M.C., V.G.M., H.W., and G.J.J. Writing—original draft: J.W., H.W., and G.J.J. Writing—review and editing: J.W., M.W., V.G.M., P.D.D., H.W., and G.J.J. Software: J.W., and P.D.D. Resources: M.C., P.D.D., H.W., and G.J.J. Visualization: J.W., M.W., H.W., and G.J.J. Supervision: V.G.M., P.D.D., H.W., and G.J.J. Project administration: P.D.D., H.W., and G.J.J. Funding acquisition: V.G.M., M.C., P.D.D., H.W., and G.J.J. **Competing interests:** H.W. is a cofounder and chair of the scientific advisory board of Ventus Therapeutics. The remaining authors declare that they have no competing interests. **Data, code, and materials availability:** All data and code needed to evaluate and reproduce the results in the paper are present in the paper and/or the Supplementary Materials. Representative cryo-tomograms reported in this study have been deposited in the Electron Microscopy Data Bank (EMDB) under accession codes EMD-75244, EMD-75245, EMD-75246, EMD-75247, EMD-75248, EMD-75249, and EMD-75250. New materials generated in this study, including the mSL-NLRP3 THP1 cell line, plasmids, and supplemental reagents, are available from the corresponding author, H.W. (wu@crystal.harvard.edu), subject to scientific review and a completed material transfer agreement. Scripts generated in this study for correlative microscopy are publicly available on GitHub at the following link: https://github.com/pdahlb/trico_softwaresuite and are permanently archived in the Stanford Digital Repository under the accession link: https://purl.stanford.edu/dw434qk4516.

Submitted 9 December 2025
Accepted 24 February 2026
Published 27 March 2026
10.1126/sciadv.aee2473